NAVIER-STOKES COMPUTATIONS OF HELICOPTER ROTOR FLOW FIELDS

A THESIS SUBMITTED TO
THE GRADUATE SCHOOL OF NATURAL AND APPLIED SCIENCES
OF
MIDDLE EAST TECHNICAL UNIVERSITY

BY

ALİ OĞUZ YÜKSEL

IN PARTIAL FULFILLMENT OF THE REQUIREMENTS
FOR
THE DEGREE OF MASTER OF SCIENCE
IN
AEROSPACE ENGINEERING

SEPTEMBER 2017

Approval of the thesis:

NAVIER-STOKES COMPUTATIONS OF HELICOPTER ROTOR FLOW FIELDS

submitted by **ALİ OĞUZ YÜKSEL** in partial fulfillment of the requirements for the degree of **Master of Science in Aerospace Engineering Department, Middle East Technical University** by,

Prof. Dr. Gülbin Dural Ünver
Dean, Graduate School of **Natural and Applied Sciences** _____

Prof. Dr. Ozan Tekinalp
Head of Department, **Aerospace Engineering** _____

Prof. Dr. Yusuf Özyörük
Supervisor, **Aerospace Engineering Department, METU** _____

Examining Committee Members:

Prof. Dr. Serkan Özgen
Aerospace Engineering Department, METU _____

Prof. Dr. Yusuf Özyörük
Aerospace Engineering Department, METU _____

Prof. Dr. Ünver Kaynak
Mechanical Engineering Department,
TOBB University of Economics and Technology _____

Assist. Prof. Dr. Ali Türker Kutay
Aerospace Engineering Department, METU _____

Assist. Prof. Dr. Mustafa Kaya
Aeronautical Engineering Department,
Ankara Yıldırım Beyazıt University _____

Date: _____

I hereby declare that all information in this document has been obtained and presented in accordance with academic rules and ethical conduct. I also declare that, as required by these rules and conduct, I have fully cited and referenced all material and results that are not original to this work.

Name, Last Name: ALİ OĞUZ YÜKSEL

Signature :

ABSTRACT

NAVIER-STOKES COMPUTATIONS OF HELICOPTER ROTOR FLOW FIELDS

Yüksel, Ali Oğuz
M.S., Department of Aerospace Engineering
Supervisor : Prof. Dr. Yusuf Özyörük

September 2017, 56 pages

Helicopters are widely used for military and civilian purposes because of their unique capability of maneuvering including vertical take-off and landing. A helicopter rotor provides this capability of motion with rotating wings. Aerodynamic forces on rotor blades generate the thrust and torque. Hence, it is significant to predict pressure distributions on rotor blades in hover, climbing, descending, and forward flight, for assessing the helicopter performance. Not only this but acoustic radiation from helicopter rotors also depends on the rotor load distributions. Motivated by these points, the objective of the thesis is to carry out flow solutions of helicopter rotors in hover and forward flight. The thesis involves numerical solutions of both Euler and Reynolds-Averaged Navier-Stokes equations. Commercial software, Ansys Fluent is used together with its User Defined Function capability to handle moving meshes. To assess the success of User Defined Function capability for providing cyclic motion, comparisons with analytical blade motion are carried out. Then, numerical flow solutions over rotor blades are compared with available experimental and numerical results from literature. Results indicate good agreement. Aerodynamic load distributions on rotating blades and flow field solutions around some of the computed rotors are also used as input into a noise prediction code developed under a separate work which has been supported by the Turkish Aerospace Industry, Inc. Rotary Wing Technological Center. Sound pressure levels predicted employing the flow solutions obtained in this thesis are also presented.

Keywords: Aerodynamics, Computational fluid dynamics, Helicopter rotor, Hover, Forward flight, Rotor performance, Rotor noise, Cyclic motions

ÖZ

HELİKOPTER ROTORUNUN ÇEVRESİNDEKİ AKIŞIN NAVIER-STOKES HESAPLAMALARI

Yüksel, Ali Oğuz
Yüksek Lisans, Havacılık ve Uzay Bölümü
Tez Yöneticisi : Prof. Dr. Yusuf Özyörük

Eylül 2017 , 56 sayfa

Dikey iniş ve kalkışı da içeren özgün manevra kabiliyetinden dolayı helikopterler askeri ve sivil amaçlarla geniş çapta kullanılmaktadır. Bir helikopter rotoru bu hareket kabiliyetini döner kanatlarla sağlamaktadır. Rotor palleri üzerindeki aerodinamik kuvvetler itki kuvvetini ve torku üretmektedir. Dolayısıyla helikopter performansını değerlendirmek için askı, yükselme, alçalma ve ileri uçuşundayken rotor palleri üzerindeki basınç dağılımlarını tahmin etmek önemlidir. Sadece bu değil; helikopter rotorlarından kaynaklı akustik yayılma da rotorun üzerindeki yük dağılımına bağlıdır. Bu noktalardan hareketle, bu tezin amacı askı ve ileri uçuştaki helikopter rotorunun akış çözümlerini gerçekleştirmektir. Bu Tez hem Euler hem de Reynolds-Ortalanmış Navier-Stokes denklemlerinin numerik çözümlerini içermektedir. Ansys Fluent ticari yazılımı ile bunun, hareketli ağlar için gereğini yapan, Kullanıcı Tanımlı Fonksiyon kabiliyeti beraber olarak kullanılmıştır. Kullanıcı Tanımlı Fonksiyon kabiliyeti ile verilen periyodik hareketin başarısını değerlendirmek için analitik pal hareketi ile karşılaştırmalar yapılmıştır. Sonra, rotor üzerindeki numerik akış çözümleri, literatürdeki mevcut deneysel ve numerik sonuçlarla karşılaştırılmıştır. Sonuçlar iyi uyum göstermektedir. Ayrıca, bazı hesaplanmış rotorların dönen palleri üzerindeki aerodinamik yük dağılımları ve etrafındaki akış alanı çözümleri, Türkiye Uçak Sanayi A.Ş. Döner Kanat Teknoloji Merkezi destekli ayrı bir çalışma altında geliştirilen bir gürültü hesaplama kodunda girdi olarak kullanılmıştır. Bu tezde elde edilen akış çözümleri

kullanılarak hesaplanan ses basınç seviyeleri de sunulmaktadır.

Anahtar Kelimeler: Aerodinamik, Hesaplamalı akışkanlar dinamiği, Helikopter rotoru, Askı uçuşu, İleri uçuş, Rotor performansı, Rotor gürültüsü, Periyodik hareketler

Dedicated to those who bequeathed scientific education to us.

ACKNOWLEDGMENTS

I would like to express my greatest gratitude to my supervisor, Prof. Dr. Yusuf Özyörük, for his highly valuable guidance and constructive feedback during this dissertation. His profound insights into aeroacoustics and fluid dynamics have always helped me.

I would like to express my sincere thanks to my dear parents, Ayfer and Ersin, my brother Onur for their endless love, patience and support throughout my life. Also, I would like to thank my sweetheart Özge Arı who always try to stand by me with her peerless kindness.

I would like to thank my manager Hakan İşçi and my chief Murat Ceyhan for their supports to my participation in AIAA Scitech 2016. I would like to thank my friends, Osman Güngör and Mete İnekçi for their efforts to help me to overcome the problems I have encountered. I would like to thank Tolga Güzel for his help regarding hpc cluster system. Also, I would like to thank best colleagues ever for joyful times in Devrim and running evenings.

This thesis is supported by Undersecretariat for Defence Industries (SSM), Turkish Aerospace Industries, Inc. (TAI) through Rotary Wing Technology Center (DKTM).

TABLE OF CONTENTS

LIST OF TABLES

TABLES

LIST OF FIGURES

FIGURES

LIST OF ABBREVIATIONS

FW-H	Ffowcs Williams–Hawkings
HSI	High Speed Impulsive
CFD	Computational Fluid Dynamics
TAI	Turkish Aerospace Industries, Inc.
DKTM	Rotary Wing Technology Center
RANS	Reynolds Averaged Navier Stokes
MRF	Moving Reference Frame
VTM	Vorticity Transport Models
FVM	Finite Volume Method
UDF	User Defined Function
PBCS	Pressure Based Coupled Solver
FMG	Full Multigrid Initialization
MUSCL	Monotone Upstream-Centered Schemes for Conservation Laws
Ω	Angular velocity
R	Rotor radius
V_f	Forward flight velocity
ψ	Azimuth angle
M	Mach number
M_f	Forward flight Mach number
$M_{hover,tip}$	Tip Mach number of hovering rotor
M_{tip}	Tip Mach number
V_{tip}	Tip velocity
r	Radial location on the blade, measured from the center of rotation (r=0) to the blade tip (r=R, or non-dimensional r=1)
μ	Advance ratio
N	Number of blades
T	Static Temperature
c_s	Speed of sound
b	Blade number

θ	Blade pitch angle, positive nose upward
β	Blade flap angle, positive upward
ϕ	Blade lead-lag angle, positive as lead
θ_0	Collective angle
β_0	Conning angle
θ_{1c}	Lateral cyclic pitch angle
β_{1c}	Longitudinal cyclic flap angle
ϕ_{1c}	Lateral shift angle
θ_{1s}	Longitudinal cyclic pitch angle
β_{1s}	Lateral flap angle
ϕ_{1s}	Longitudinal shift angle
t	Time
c	Chord

CHAPTER 1

INTRODUCTION

1.1 Fundamentals of Rotor Aerodynamics

Helicopters are aircraft that utilize rotating wings to produce forces in all directions and keep control [7]. Creating forces in all directions and keeping control provide more maneuverability than fixed-wing aircraft. The capability of maneuvering makes helicopters unique aircraft. A variety of flight missions cannot be performed by fixed-wing aircraft. In other words, helicopters are indispensable for a lot of operations. Therefore, a helicopter plays crucial role in civil and military operations.

Helicopter motions might in general be categorized as climbing, descending, hovering, forward flight, and maneuvering, which combine all possible motions. In the thesis, aerodynamic flow fields of helicopter rotors both in hover and forward flight are examined. Some fundamental characteristics of helicopter rotor flow fields are discussed below.

1.1.1 Principles of Hover and Forward Flight

Angle of attack and dynamic pressure at every sections of the blade decide on creation of the forces and moments of the rotor including lifting capability. Figure 1.1 illustrates an example of a rotor both in hover and forward flight [1]. By convention, blade azimuth angle defining the angular blade position is zero in the tail direction, and direction of rotation is counter-clockwise when observed from top. In the light of this information, velocity normal to the leading edge is radially linear and it does

not change with azimuthal position in hover. In other words, velocity at the rotor hub is minimum and it equals to zero; while velocity at the blade tip is maximum and it equals to ΩR. In forward flight, velocity normal to the leading edge is also radially linear. However, it changes with azimuthal position unlike that in hover condition. Velocity at rotational axis is equal to free-stream velocity. Maximum velocity normal to the leading edge occurs at the advancing side which corresponds to an azimuth angle of 90 degrees. On the other hand, minimum velocity normal to the leading edge appears at the retreating side which corresponds to an azimuth angle of 270 degrees. Therefore, it can easily be inferred that blade tip velocity relative to a fixed frame (e.g. ground) is equal to $\Omega R + V_f sin(\psi)$. In the example of forward flight shown in Figure 1.1 [1], hover tip Mach number is equal to 0.6, and advance ratio ($M_f/M_{hover,tip}$) is equal to 0.3.

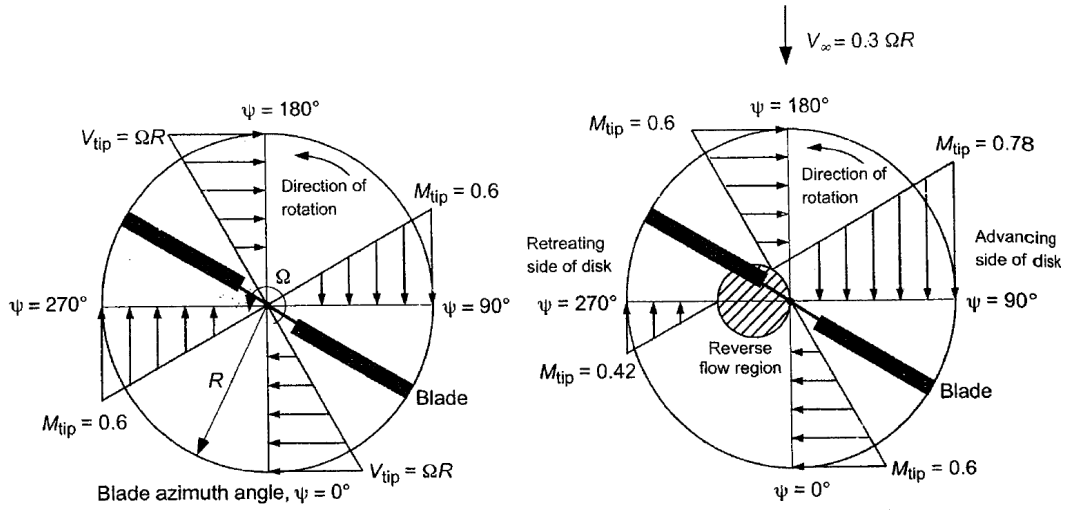

Figure 1.1: Velocity normal to the leading edge for both hovering rotor (left) and rotor in forward flight (right) [1]

1.1.2 Aerodynamic Issues around Helicopter Rotor

The major complication of rotating-wing aircraft different from fixed-wing one is related to the effects of vortices trailed from each blade on rotor flow field. These vortices are strong, and have complicated structures. Also, trajectories of tip vortices have significant effect on rotor aerodynamics. Due to their rotation, rotor blade sections near the tips generate more aerodynamic forces than inner ones, while fixed

wing aircraft have nearly uniform loading along wingspan. Hence, stronger and more complicated vortices might appear around tip of rotating wing aircraft than that of fixed-wing ones. Flow paths of tip vortices of rotating wings are also distinct from those of fixed-wings. For fixed-wing aircraft, directions of the wake and tip vortices are downstream of the aircraft. On the other hand, wake and tip vortices of helicopter rotors in forward flight interact with other rotor blades for a few rotations [1]. Thus, blade-tip vortex interactions and complicated structures of tip vortices are main phenomena regarding rotor aerodynamics. In complete helicopter aerodynamics, some other interactions might also appear such as rotor wake-empennage interactions, tip vortices-tail rotor interactions.

In forward flight with high free-stream Mach number, additional problems emerge during flight. Advancing and retreating sides of rotor are related to these additional problems. Blade tip on advancing side of rotor is exposed to transonic flow. As a result of transonic flow, compressibility zones and shock waves take place at advancing side of rotor. Shock waves also cause high-speed impulsive noise, a significant component of noise. While, blade on retreating side is required to achieve higher angle of attack because of low local dynamic pressure. If angle of attack is increased over stall limit at relatively high speed forward flight, reduction in lift, and instability might arise. Also, reverse flow, a flow from trailing edge to leading edge, appears near the blade root on retreating side as explained in Section 1.1.4.

Unsteady, viscous dominated, subsonic and transonic aerodynamics interactions, and asymmetric blade normal velocity in forward flight make rotor flow field complicated. Wake structures expanded from the rotor blades continue to stay in near field of the rotor and helicopter body, producing unsteady aerodynamic loading. Therefore, accurate prediction of rotor dynamics (e.g. cyclic blade motions), wake geometry consisting of interactions (e.g. surface-vortex) play a vital role in unsteady helicopter aerodynamics [8].

1.1.3 Noise generation of helicopter rotors

Aeroacoustics is concerned with pressure waves and their propagation in air. The complexity of helicopter aeromechanics have caused late improvements in study of

helicopter aeroacoustics when compared with fixed wing aircraft. These improvements include the understanding of source mechanisms of noise, and the development of feasible and accurate prediction techniques based on the flow physics. Moreover, fixed wing aircraft can utilize noise control with the help of tools such as engine acoustic liners. Physically, helicopters cannot use these tools. Therefore, aeroacoustic studies on helicopter noise are based only on source noise reduction [9].

Integrating the Ffowcs Williams-Hawkings (FW-H) equation is widely used to predict helicopter rotor noise. The classification of noise components might be defined as linear aerodynamics and nonlinear effects. Thickness and loading noise components are examined by monopole and dipole source terms of the FW-H equation, respectively. High speed impulsive (shock, HSI) noise involves quadrupole source terms. While computations of thickness noise components need only blade kinematic motion history, the loading noise and shock noise components also require the flow variables. Thus, Computational Fluid Dynamics (CFD) solution is required as input to predict the noise. In this thesis, flow variables attained are used as input by noise prediction code developed under a TAI/DKTM project, specifically to compute noise of a hovering TAI whirl tower rotor with a tip Mach number of 0.49. Furthermore, HSI noise component of untwisted experimental UH-1H rotor with a tip Mach number of 0.88 is computed by the code using the CFD solutions obtained in this thesis.

1.1.4 Reverse flow

A reverse flow region takes place on the rotor on the retreating side near the rotation axis because of the asymmetric velocity normal to leading edge in forward flight. In this region, direction of velocity with respect to the blade is from trailing edge to leading edge. On the retreating side of the disk, direction of the rotational velocity is from leading edge to trailing edge. However, direction of free stream velocity is from trailing edge to leading edge. Hence, reverse flow is located in the region where free stream velocity is greater than rotational velocity. The circular diameter of the reverse flow region depends on the advance ratio. At an azimuth angle of 270 degrees, velocity normal to leading edge is zero when $V_{tip}(r - \mu)$. Hence, $R\mu$ is the diameter of reverse flow region. The effect of reverse flow is limited when the advance ratio

is low. In contrast, the effect of reverse flow is significant as advance ratio is higher than 0.5 [7]. Although reverse flow region is located where local dynamic pressure is low, it has marked effects on the flow field.

1.1.5 Periodic motions of blade

Rotor is exposed to asymmetric normal velocity in forward flight, as explained in Figure 1.1. On the advancing side of the rotor disk, flow velocity and local dynamic pressure are greater than those on the retreating side of the disk. As a result of this, thrust and moment generations are different for each side of disk. An instability exists if the imbalances of thrust and moment are not eliminated. In order to remove the imbalance, a cyclic motion is given to the blade. Periodic motions of the blade which are flapping, pitching (feathering) and lead-lag are illustrated in Figure 1.2, where also shown are the typical hinge locations and axes.

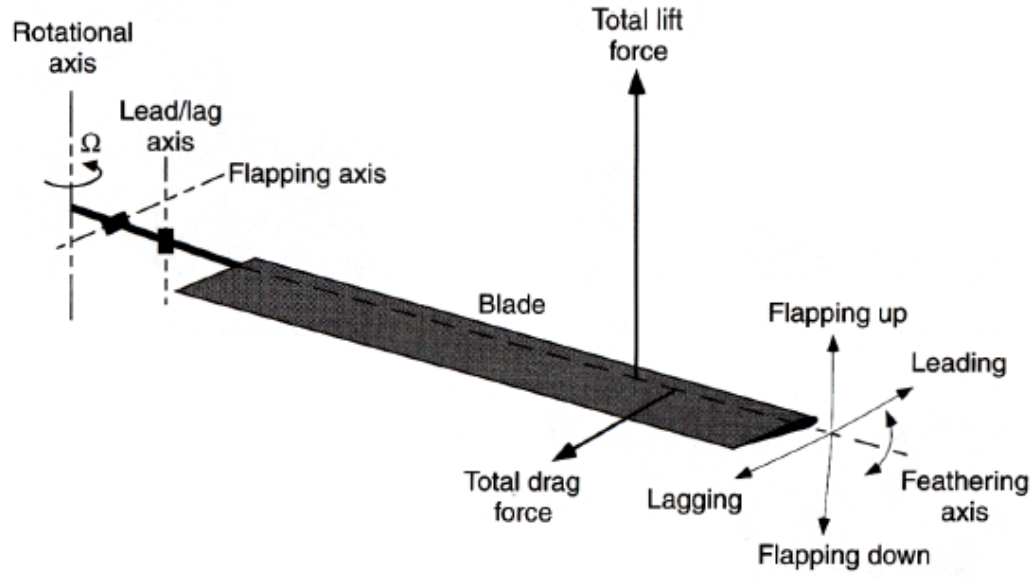

Figure 1.2: Cyclic motions of blade [1]

Azimuthal position may be represented by a function that depends on time and angular velocity of the rotor. The period of the cyclic motions of a blade is equal to $2\pi/\Omega$ seconds. On the other hand, the period of the rotor is $2\pi/(\Omega N)$ seconds. In other words, position of a rotor blade at an arbitrary time is the same as that after $2\pi/(\Omega N)$ seconds. Thus, the flapping, feathering, and led-lag angles are also periodic func-

tions of the azimuth angle. Furthermore, these periodic functions might be described by Fourier series. Therefore, flapping, feathering, and led-lag are described by the Fourier series given in Section 2.5.

1.2 CFD Modelling of Helicopter Rotors in Hover and Forward Flight

In the early times of rotorcraft development, aerodynamic design had been based on empirical results, and mathematical models such as momentum and blade element theory. Then, increase in computer memory and speed led to development of computational fluid dynamics (CFD) techniques. Caradonna [10] states that CFD is a tool which is both readily accessible for industry and reliable to design rotorcraft. Although CFD is a reliable tool to design rotorcraft, there are a lot of sources of error that must be considered carefully. Sources of errors are round-off errors, convergence errors, discretization errors, and model errors. Thus, it is significant to be aware of the error sources, and limitations of CFD for the sake of predictions regarding rotor flow field.

The main purpose of the design of rotorcraft is to reach maximum performance in hover and forward flight; furthermore, minimum noise and vibration are demanded [10]. CFD modelling can be involved in design process with accurate flow solutions. CFD analysis might calculate the effects of parameters such as aspect ratio, twist, conning, collective and cyclic angles on helicopter rotor performance. These reliable calculations are incorporated into the early phase of design process. Therefore, experimental cost decreases, and efficient design process is obtained as industry demands. Also, aeroacoustic predictions utilize computations of the rotor flow fields. It is widely known that aeroacoustics is a critical subject in helicopter industry because certification criteria regarding noise restrictions are getting more intolerant by time. Aeroacoustic noise, in general, can be divided into three main components which are thickness noise, loading noise, and shock-associated noise. Kinematic knowledge on blade motion during an arbitrary flight is enough to calculate thickness noise. On the other hand, loading and shock-associated noise require solutions of the flow field. Loading noise needs aerodynamic loads on the surfaces of rotor blades, while shock-associated noise needs flow field around rotor. Thus, CFD applications on helicopter

rotor could be used as input for prediction of helicopter rotor noise. The following sections briefly explain some computational methods used in rotorcraft problems. Assumptions and limitations of methods are also stated. Solutions of the Reynolds-Averaged Navier-Stokes (RANS), and Euler equations are employed in the thesis, and they are explained in Section 2.1. Moving Reference Frame (MRF) used in steady state solutions of hover cases is discussed below.

1.2.1 Moving reference frame

Moving reference frame (called as MRF) method is independent of flow equations which is intended to be solved. For instance, MRF is applicable to potential flow theory as well as Navier-Stokes equations. The method is based on solving flow equations with respect to a moving reference frame, instead of a stationary frame. As viewed from the blade-fixed frame, the problem turns into a time-independent flow problem. Therefore, the governing equations of the flow field around the helicopter rotor can be solved in a steady state way. There is a limitation on the application of MRF to flow equations around helicopter rotor. Rotor blades must not have cyclic motion such as feathering, flapping, and lead-lag. Hence, hover and forward flight cases without cyclic motion can be solved theoretically by MRF method. Solving the equations of fluid flow in a rotating frame rather than inertial frame has important advantages for hovering rotor. Convergence time of solution in rotating frame is significantly less than that in stationary frame. Moreover, using rotating frame does not need remeshing in each time step unlike using stationary reference frame [11]. Srinivasan and Baeder [12] presented a work regarding helicopter rotor flow fields including the solutions of the equations written in rotating frame. In their work, helicopter rotor aerodynamic flow fields are calculated by applying MRF method.

1.2.2 Vorticity Transport Models

The effects of blade-wake and wake-wake interactions on the aerodynamic loading, acoustics and vibration have significant results for rotorcraft. In order to capture the complexities in the interactions, vorticity transport model (VTM) can provide the

computational solutions of flow field. This method employs a direct computational solution of incompressible Navier-Stokes and Biot-Savart relationship to calculate evolution of the wake structure. Brown [13] states that developed model is a computational helicopter rotor wake model which is based on the numerical solutions of time-dependent fluid dynamic equations governing the generation and convection of vorticity over a domain surrounding the rotor. When compared to Navier Stokes solutions, VTM provides more feasible approach to predict rotor wake. Although this method presents the complete model for the evolution of rotor wake, it is computationally expensive, similar to mesh based CFD approaches, for use in parametric design procedure [1]. Besides, Free vortex method (FVM), a simplified form of VTM, also predicts evolution of the rotor wake. In a lot of practical problems, length scales of rotor wake structures generated by viscous effects can be much smaller when compared to structures caused by purely potential flow. In these cases, FVM is appropriate way to predict rotor wake structure [1]. A drawing of total wake in hovering rotor and typical blade loading distribution is illustrated in Figure 1.3 [2].

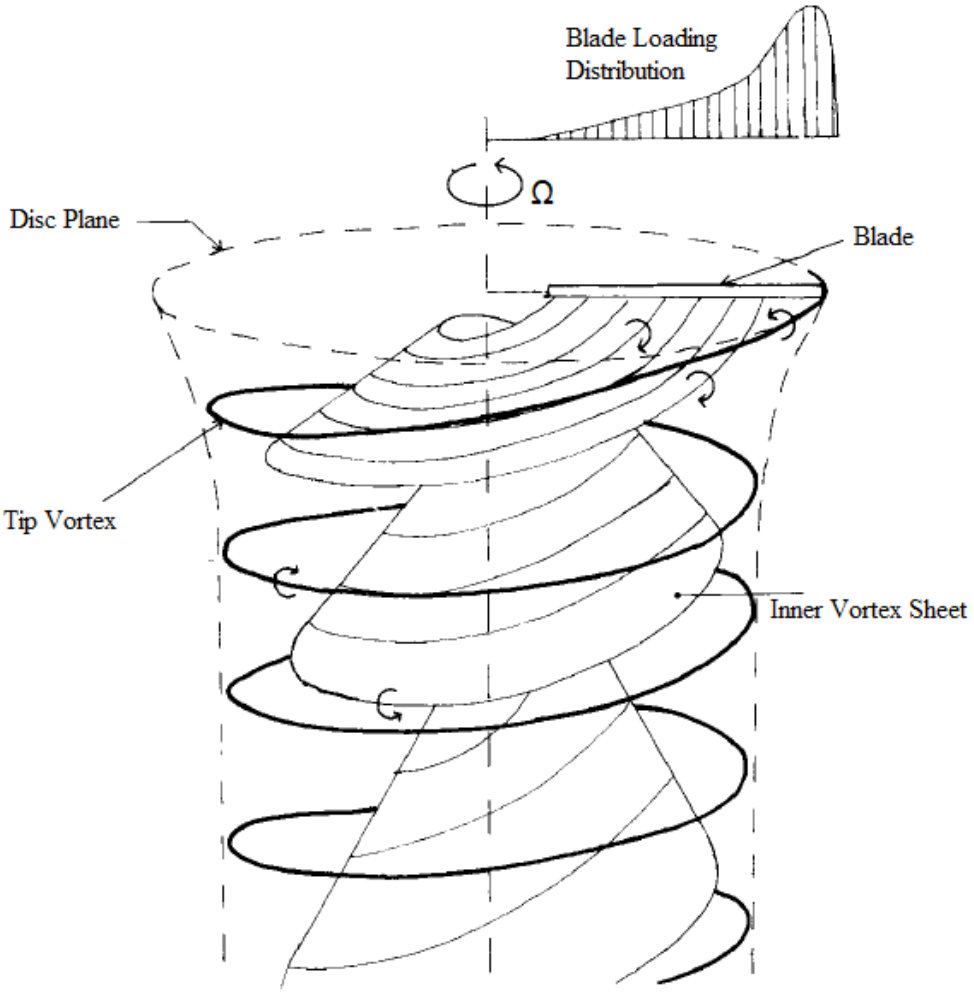

Figure 1.3: Total wake in hover and blade loading distribution on a blade [2]

1.2.3 Boundary Layer Equations

Boundary layer equations offer intermediate solution between Navier-Stokes and Euler equations. Viscous effects are only considered in boundary layer. Outside the boundary layer, inviscid or potential flow solutions are applied. Hence, aerodynamic loads and flow field are predicted with a feasible numerical method generally called as viscous-inviscid interaction technique. One of the early and important examples of the applications of boundary layer equations to helicopter flow field was performed by Srinivasan and McCroskey [14]. In their work, unsteady, thin layer Navier-Stokes equations written in rotor coordinates are solved to predict flow fields of a hovering rotor at subsonic, transonic, lifting and non-lifting conditions. The procedure

of solution is first to solve inviscid flow field and then to solve the boundary layer equations. After performing a correction to consider the effect of the thickness of the boundary layer on the outer flow, the inviscid solution is then repeated. The resultant solution provides a high Reynolds number solution to the Navier-Stokes equations [1]. Boundary layer equations give inaccurate results where greatly seperated flows occur. Hence, regions of seperated flow must be considered before boundary layer approach is employed.

1.3 Objective of Thesis

The main objective of the thesis is to carry out flow solutions of isolated helicopter rotors in both hover and forward flight. Forward flight case with cyclic motions of blade is relatively more challenging than the others because of blade motions and effects of unsteady aerodynamics. Therefore, numerical cyclic motions in each time step must match with analytical motions, and flow solutions must capture the unsteady effects in that case. The resultant flow variables on the rotor blade surfaces and around the entire rotor are employed for noise prediction by a code developed under a TAI/D-KTM project [4]. The aim is to obtain resultant pressure distributions on the blades, as well as integrated results of them, namely rotor performance data (e.g. thrust and torque). Results indicate good comparisons for both performance data and sound pressure levels with available experimental and numerical results in literature.

1.4 Scope of Thesis

The thesis includes the solutions of both Euler and Reynolds-Averaged Navier-Stokes equations in hover and forward flight. Hover computations are carried out in a steady state way by employing the MRF method. On the other hand, forward flight simulations are performed in a time-dependent manner. Commercial software, Ansys Fluent v17.0 is used together with its User Defined Function (UDF) capability. In hover cases, Caradonna-Tung rotor [3], a rotor tested in the TAI whirl tower facility [15], and non-lifting and untwisted UH-1H rotor with transonic flight conditions are investigated [16]. In forward flight cases, a two-bladed Onera model rotor without

cyclic motions of blade and Caradonna-Tung rotor with cyclic motions of blade are examined [5]. To assess the success of UDF for giving cyclic motions, comparisons with analytical blade motions are carried out. Performance curves, the change of non-dimensional thrust and torque with collective angles, chordwise pressure distributions at different spanwise sections and sound pressure levels are compared with the experimental and available numerical results from literature.

CHAPTER 2

METHODOLOGY

2.1 Governing Flow Equations of Aerodynamics

Three dimensional, compressible, Reynolds-Averaged Navier-Stokes (generally known as RANS) equations are used as the governing equations for aerodynamic fields of helicopter rotors. Numerical solutions to the RANS equations are obtained for the Caradonna and Tung [3] rotor in hover, TAI whirl tower rotor [15] in hover, Onera two-bladed model rotor in forward flight without cyclic motions of blade and Caradonna and Tung rotor in forward flight with cyclic motions of blades [5]. In hovering UH-1H rotor with transonic flight conditions case, compressible Euler equations are used as the governing equations.

Three-dimensional, compressible RANS equations (Favre-averaging) in Cartesian coordinates could be represented as follows [17].

$$\frac{\partial Q}{\partial t} + \frac{\partial (D - D_{vis})}{\partial x} + \frac{\partial (E - E_{vis})}{\partial y} + \frac{\partial (F - F_{vis})}{\partial z} = 0 \tag{2.1}$$

Conservative flow variable vector, Q is given as follows.

$$Q = \begin{Bmatrix} \bar{\rho} \\ \bar{\rho}\widetilde{u} \\ \bar{\rho}\widetilde{v} \\ \bar{\rho}\widetilde{w} \\ \bar{\rho}\widetilde{e}_t \end{Bmatrix} \tag{2.2}$$

Inviscid flux vectors (D, E, F), and viscous flux vectors (D_{vis}, E_{vis}, F_{vis}) can be written as

$$
\mathrm{D}=\begin{Bmatrix} \bar{\rho}\widetilde{u} \\ \bar{\rho}\widetilde{u}^2+\bar{P} \\ \bar{\rho}\widetilde{u}\widetilde{v} \\ \bar{\rho}\widetilde{u}\widetilde{w} \\ (\bar{\rho}\widetilde{e}_t+\bar{P})\widetilde{u} \end{Bmatrix}, \mathrm{D}_{vis}=\begin{Bmatrix} 0 \\ \bar{\tau}_{xx} \\ \bar{\tau}_{xy} \\ \bar{\tau}_{xz} \\ \bar{\tau}_{xx}\widetilde{u}+\bar{\tau}_{xy}\widetilde{v}+\bar{\tau}_{xz}\widetilde{w}-\bar{q}_x \end{Bmatrix}
$$

$$
\mathrm{E}=\begin{Bmatrix} \bar{\rho}\widetilde{v} \\ \bar{\rho}\widetilde{v}\widetilde{u} \\ \bar{\rho}\widetilde{v}^2+\bar{P} \\ \bar{\rho}\widetilde{v}\widetilde{w} \\ (\bar{\rho}\widetilde{e}_t+\bar{P})\widetilde{v} \end{Bmatrix}, \mathrm{E}_{vis}=\begin{Bmatrix} 0 \\ \bar{\tau}_{yx} \\ \bar{\tau}_{yy} \\ \bar{\tau}_{yz} \\ \bar{\tau}_{yx}\widetilde{u}+\bar{\tau}_{yy}\widetilde{v}+\bar{\tau}_{yz}\widetilde{w}-\bar{q}_y \end{Bmatrix} \tag{2.3}
$$

$$
\mathrm{F}=\begin{Bmatrix} \bar{\rho}\widetilde{w} \\ \bar{\rho}\widetilde{w}\widetilde{u} \\ \bar{\rho}\widetilde{w}\widetilde{v} \\ \bar{\rho}\widetilde{w}^2+\bar{P} \\ (\bar{\rho}\widetilde{e}_t+\bar{P})\widetilde{w} \end{Bmatrix}, \mathrm{F}_{vis}=\begin{Bmatrix} 0 \\ \bar{\tau}_{zx} \\ \bar{\tau}_{zy} \\ \bar{\tau}_{zz} \\ \bar{\tau}_{zx}\widetilde{u}+\bar{\tau}_{zy}\widetilde{v}+\bar{\tau}_{zz}\widetilde{w}-\bar{q}_z \end{Bmatrix}
$$

Flow variables are seperated into averaged and fluctuating components. Overbar and tilde signs indicate the Reynolds-averaging and Favre-averaging, respectively. Reynolds and Favre averagings of an arbitrary flow variable, ϕ could be written as

$$
\bar{\phi}=\frac{1}{t}\int_t^{t+\Delta t}\phi dt \tag{2.4}
$$

$$
\widetilde{\phi}=\frac{\bar{\rho}\bar{\phi}}{\bar{\rho}} \tag{2.5}
$$

Total energy term with Favre-averaging, $\widetilde{e}_t$, is defined as

$$
\widetilde{e}_t=\frac{\bar{P}}{\bar{\rho}(\gamma-1)}+\frac{1}{2}(\widetilde{u}^2+\widetilde{v}^2+\widetilde{w}^2) \tag{2.6}
$$

Compressible Euler equations are obtained by omitting viscous flux vectors (D_{vis}, E_{vis}, $Fvis$) from compressible Navier-Stokes equations. Euler equations are considered as feasible in certain flow physics that turbulence and viscous effects are not significant. High Reynolds number flows over helicopter rotors are commonly considered as convenient for solution of Euler equations.

2.2 Solution Strategy and Solver

Solvers in Ansys Fluent commercial code solve the governing equations, conservation of mass, momentum, energy in integral forms, and scalar turbulence equation. Control volume based technique is employed. Solution domain is divided up into discrete control volumes using a computational grid. Integration of the governing equations on control volumes is carried out in order to build algebraic equations for the discrete flow variables. Discretized equations are linearized. The resulting linear equation system is solved to provide updated values of the flow variables [18]. Cell-centered finite volume method is used as discretization algorithm. Linearization and solution of the system of equations is performed by pressure based coupled solver (PBCS). Although pressure-based solvers are initially used for incompressible flows, the new modified versions of pressure-based solvers are applicable for a wide range of flow regimes, from low speed incompressible flow to high-speed compressible flow. In this thesis, PBCS is employed because it decreases the time to reach convergence, approximately as much as five times faster, by solving momentum and pressure-based continuity equations in a coupled way. Although PBCS requires about 2 times more memory, its advantages outweigh the weaknesses. Pseudo-transient solution method is a kind of implicit under relaxation method for simulations in steady-state. It decreases the convergence times and provides more robust solutions on relatively highly skewed grids. In practice, average speedups of steady state solution to reach convergence is 30 percent to 50 percent [19]. Also, initialization is a significant process to reach converged solution faster. Full multigrid initialization (FMG) is used to achieve feasible initial solution as considered the overall solution time. The necessary time for FMG is longer than other types of initialization. However, it helps to obtain converged solution faster by better first estimation. FMG solves Euler equations, and it

is convenient for compressible and external flows.

2.3 Boundary Conditions

2.3.1 Wall Boundary Conditions

Wall boundary conditions are employed to bound fluid and solid fields on blade surfaces. For Euler solution presented in Sections 3.1.3, inviscid wall boundary conditions are applied. Velocity normal to wall is zero, $\vec{V}.\vec{n} = 0$. Velocity vector is tangent to blade wall (flow-tangency). For Navier-Stokes solutions presented in Sections 3.1.1, 3.1.2, 3.2.1,3.2.2, fluid sticks to the wall and moves with the same velocity with the wall (no-slip condition). Wall boundaries are stationary in hover cases, while they move with adjacent cell zone in forward flight cases. Adiabatic wall condition is applied; In other words, heat flux between air and wall is equal to zero. Moreover, wall roughness and roughness height are specified for viscous cases.

2.3.2 Far-field Boundary Conditions

As outer boundary conditions, pressure far-field boundary conditions are employed. Free stream Mach number, direction of flow, static temperature and pressure are defined. The turbulence viscosity ratio, $\frac{\mu_t}{\mu}$, at the far-field boundary are also defined for viscous solutions. Critical point is that boundaries must be located at far enough from the rotor. For instance, distances between rotation center and boundaries located at sides and top are 10 rotor radii. The bottom boundary is placed away from the rotation center by 15 rotor radii distance for lifting case. Rotor is placed in the middle of bottom and top boundaries for non-lifting cases.

2.3.3 Periodic Boundary Conditions

Periodic boundary conditions can theoretically be implemented for all hover cases, because flow rotationally and periodically repeats. Flow variables coming in one periodic surface are exactly same as the ones coming out the other periodic surface.

Hence, periodic boundaries must be used in pairs. However, forward flight cases with or without cyclic motion are not convenient to apply periodic boundary conditions. The flow fields in forward flight cases do not have a periodically repeating nature.

Periodic conditions could allow smaller solution domains. Hence, number of cells can be increased for better resolution. Therefore, better resolution can be obtained with same computational power.

2.4 Discretizations of the Equations

Hover simulations, in Section 3.1 are carried out in steady state manner as stated earlier. Hence, the equations are only exposed to spatial discretization. On the other hand, forward flight simulations, in Section 3.2 are solved in time-dependent manner. Therefore, spatial and temporal discretization are applied to the equations of forward flight cases.

Third order MUSCL scheme is used by combining second order upwind with central differencing scheme. Second order upwind scheme can be given as follows.

$$\varphi_{f,sou} = \varphi + \nabla\varphi.\vec{r} \tag{2.7}$$

φ is the scalar discrete quantity at an arbitrary cell center. $\nabla\varphi$ is the gradient at the upstream cell. $\vec{r}$ is the vector pointing to corresponding face centroid from centroid of upstream cell. In central differencing scheme, an arbitrary scalar quantity is determined as

$$\varphi_{f,cd} = 0.5(\varphi_0 + \varphi_1) + 0.5(\nabla\varphi_0.\vec{r}_0 + \nabla\varphi_1.\vec{r}_1) \tag{2.8}$$

Neighbour cells, 0 and 1, are split by face f. Direction of the $\vec{r}$ is from cell center to face center. Hence, the following equation illustrates the third order MUSCL scheme written by coupling second order upwind and central differencing scheme.

$$\varphi_f = \vartheta\varphi_{f,cd} + (1-\vartheta)\varphi_{f,sou} \tag{2.9}$$

Forward flight cases are time-dependent simulations. Thus, the governing equations of these cases require discretization in both time and space. First order implicit transient formulation is employed as illustrated in Equation 2.10. Time derivative of a scalar variable φ is shown in Equation 2.11.

$$\frac{\varphi^{n+1} - \varphi^{n}}{\Delta t} = F(\varphi^{n+1}) \tag{2.10}$$

$$\frac{\delta \varphi}{\delta t} = F(\varphi) \tag{2.11}$$

2.5 Implementation of the Prescribed Periodic Motions of Blade

Periodic motions of blade are explained briefly in Section 1.1.5. In this section, periodic motions of blade are examined in a detailed way. Also, application of periodic motions of blade to CFD analysis is described. Results of simulation case including periodic motions are demonstrated in Section 3.2.2.

Periodic motions of blade are provided by User Defined Function [UDF] in Fluent software. UDFs are functions in C programming language that can dynamically be loaded with Fluent. They are used in order to enhance standard features of commercial software, Ansys Fluent [18]. There are a lot of UDFs for a variety of purposes. In this thesis, "Define cg motion" macro is used. Rigid body motion is given for certain cell zones by this macro. Hence, cells in dynamic zones move rigidly with respect to angular and linear velocities defined in macro.

The application of periodic motions of blade to CFD simulation is as follows. Flapping, feathering and lead-lag motions are given to blade and boundary layer rigidly by UDF. Rotor rotation is provided by mesh motion in Fluent for all cell zones including blade, boundary layer and outer of the boundary layer. As blade and boundary layer perform flapping and lead-lag, cells located in outer of the boundary layer are deformed in order to avoid mesh overlapping. The application of UDF to simulation is also illustrated in Figure 2.1.

Two mesh deformation methods, which are smoothing and remeshing, are employed to the cells adjacent to the boundary layers. Spring-based smoothing is applied whose spring constant factor equals to 0.4. When constant factor equals to zero, it means that there is no damping on the springs, and boundary node motions have more effect on the motion of interior nodes. Moreover, smoothing process is performed iteratively during each time step. Number of iterations is equal to 40 in mesh smoothing. The second mesh deformation method is remeshing. When the boundary displacement is large compared to adjacent cell sizes, or cell skewness is larger than 0.95, remeshing is applied to local cells in each time step. Therefore, remeshing prevent problems such as negative cell volumes and degenerate cells.

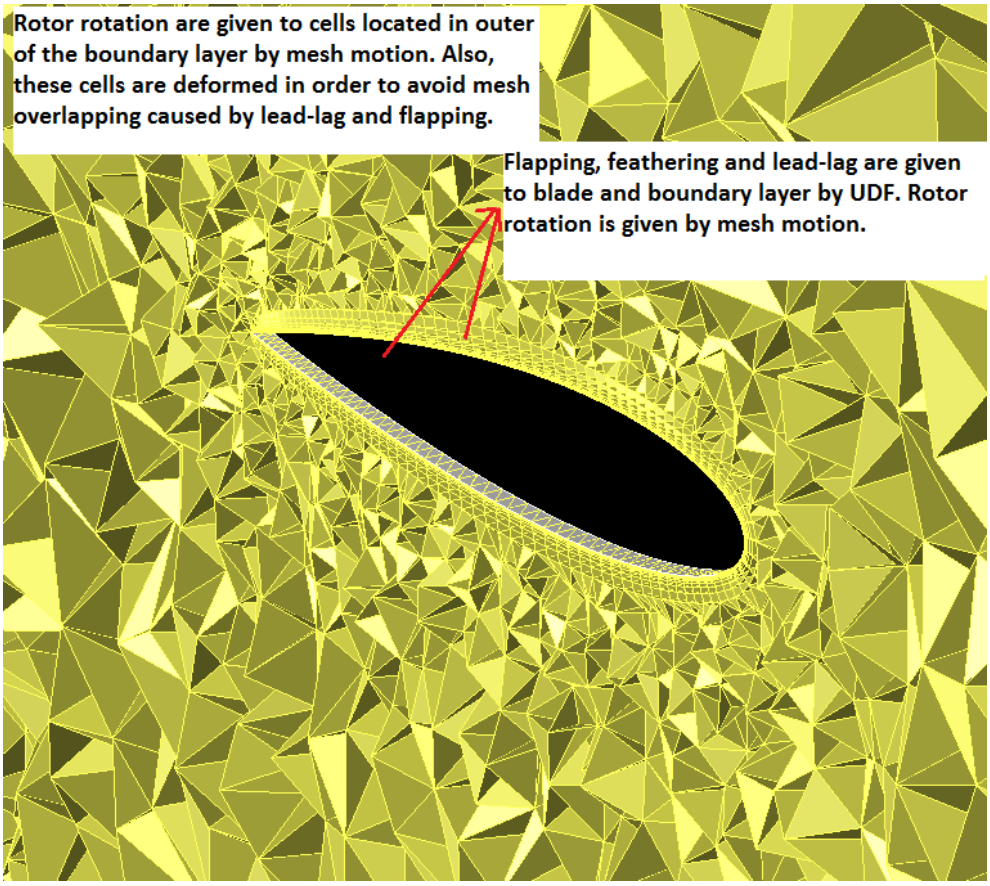

Figure 2.1: Application of periodic motions to CFD simulation

Simulation including periodic motions of blade is based on giving linear and angular velocities to cell zones at each time step. Hence, time step size affects the accuracy of motion. In order to validate the motion used in simulation, analytical calculation of

periodic blade motion is also performed. Comparisons between analytical calculation and motions performed in simulation is shown in Section 3.2.2. The first step for both analytical calculation and UDF is to define periodic motions of blade. In typical forward flight, blade performs flapping, feathering and lead-lag around specific axis as illustrated in Figure 1.2. Angles of periodic motions are feathering (θ), flapping (β) and lead-lag (ϕ). Number of blades is N and they are placed in same angular distance. Therefore, in arbitrary time, periodic motions of blade (b) is illustrated as Fourier series in the following equations.

$$\theta_b(t) = \theta_0 + \theta_{1c}\cos\psi_b + \theta_{1s}\sin\psi_b + \theta_{2c}\cos 2\psi_b + \theta_{2s}\sin 2\psi_b + ... \quad (2.12)$$

$$\beta_b(t) = \beta_0 + \beta_{1c}\cos\psi_b + \beta_{1s}\sin\psi_b + \beta_{2c}\cos 2\psi_b + \beta_{2s}\sin 2\psi_b + ... \quad (2.13)$$

$$\phi_b(t) = \phi_0 + \phi_{1c}\cos\psi_b + \phi_{1s}\sin\psi_b + \phi_{2c}\cos 2\psi_b + \phi_{2s}\sin 2\psi_b + ... \quad (2.14)$$

Here, azimuthal angle (ψ_b) is represented as a function depending on angular velocity of rotor (Ω) and time (t). Direction of the reference axis ($\psi = 0$) is from head to tail of the helicopter. First blade of rotor (b=1) is considered along reference axis at initial time. The azimuthal angle of blade b can be written as

$$\psi_b(t) = \Omega t + 2\pi(b-1)/N \quad (2.15)$$

In general, higher harmonics of feathering (θ_{2c}, θ_{2s}, etc.), flapping (β_{2c}, β_{2s}, etc.) and lead-lag (ϕ_{2c}, ϕ_{2s}, etc.) are so small and might be neglected. Therefore, periodic motion angles are simplified as.

$$\theta_b(t) = \theta_0 + \theta_{1c}\cos\psi_b(t) + \theta_{1s}\sin\psi_b(t) \quad (2.16)$$

$$\beta_b(t) = \beta_0 + \beta_{1c}\cos\psi_b(t) + \beta_{1s}\sin\psi_b(t) \quad (2.17)$$

$$\phi_b(t) = \phi_0 + \phi_{1c}\cos\psi_b(t) + \phi_{1s}\sin\psi_b(t) \quad (2.18)$$

Here, $\theta_0, \theta_{1c}, \theta_{1s}$ are collective, longitudinal and lateral pitch angles; $\beta_0, \beta_{1c}, \beta_{1s}$ are conning, lateral and longitudinal flap angles; $\phi_0, \phi_{1c}, \phi_{1s}$ are mean lag, lateral and longitudinal shifts, respectively.

In the simulation case performed in Section 3.2.2, blade is initially on the direction of helicopter tail and rotational axis is +z axis. Flapping, feathering and lead-lag hinges are located at rotational axis. The order of the cyclic motions is prescribed. It is arranged in order of rotation, flapping, lead-lag and feathering. In other words,

rotation (around z axis), flapping (around $-y^{(1)}$ axis), lead-lag (around $z^{(2)}$ axis) and feathering (around $x^{(3)}$ axis) are performed respectively.

Analytical calculation is based on coordinate transformation. For instance, x_0 is coordinate of a point on blade as time and azimuthal angle equal to zero. Therefore, coordinate transformation is carried out by the following equations.

$$\begin{bmatrix} x_1 \\ y_1 \\ z_1 \end{bmatrix} = \underbrace{\begin{bmatrix} \cos\psi & -\sin\psi & 0 \\ \sin\psi & \cos\psi & 0 \\ 0 & 0 & 1 \end{bmatrix}}_{R_1} \begin{bmatrix} x_0 \\ y_0 \\ z_0 \end{bmatrix} \tag{2.19}$$

$$\begin{bmatrix} x_2 \\ y_2 \\ z_2 \end{bmatrix} = \underbrace{\begin{bmatrix} \cos\beta & 0 & -\sin\beta \\ 0 & 1 & 0 \\ \sin\beta & 0 & \cos\beta \end{bmatrix}}_{R_2} \begin{bmatrix} x_1 \\ y_1 \\ z_1 \end{bmatrix} \tag{2.20}$$

$$\begin{bmatrix} x_3 \\ y_3 \\ z_3 \end{bmatrix} = \underbrace{\begin{bmatrix} \cos\phi & -\sin\phi & 0 \\ \sin\phi & \cos\phi & 0 \\ 0 & 0 & 1 \end{bmatrix}}_{R_3} \begin{bmatrix} x_2 \\ y_2 \\ z_2 \end{bmatrix} \tag{2.21}$$

$$\begin{bmatrix} x_4 \\ y_4 \\ z_4 \end{bmatrix} = \underbrace{\begin{bmatrix} 1 & 0 & 0 \\ 0 & \cos\theta & -\sin\theta \\ 0 & \sin\theta & \cos\theta \end{bmatrix}}_{R_4} \begin{bmatrix} x_3 \\ y_3 \\ z_3 \end{bmatrix} \tag{2.22}$$

Here, R_1, R_2, R_3, R_4 are transformation matrices and $\vec{x}_0 = [x_0, y_0, z_0]^T$ is the initial position of an arbitrary point on blade at $\psi = 0$. Therefore, after all cyclic motions of blade, final position of blade is $\vec{x}_4$ defined as.

$$\vec{x}_4 = [R_4\, R_3\, R_2\, R_1]\vec{x}_0 \tag{2.23}$$

The purpose of the analytical calculation is to prove the accuracy of motion given by commercial software and its UDF capability. After analytical calculation is performed, UDF is written in order to provide periodic motions of rotor in solver. Hence,

with certain time step interval, motion is acquired numerically. They are compared in Section 3.2.2. UDF macro provides flapping, feathering and lead-lag by using the components of angular velocity with respect to Cartesian coordinates. Therefore, it is required to define the angular velocities with respect to blade-fixed frame as follows.

$$\dot{\theta}_b(t) = -\theta_{1c}\Omega \sin\psi_b + \theta_{1s}\Omega \cos\psi_b \tag{2.24}$$

$$\dot{\beta}_b(t) = -\beta_{1c}\Omega \sin\psi_b + \beta_{1s}\Omega \cos\psi_b \tag{2.25}$$

$$\dot{\phi}_b(t) = -\phi_{1c}\Omega \sin\psi_b + \phi_{1s}\Omega \cos\psi_b \tag{2.26}$$

Angular velocities with respect to blade-fixed frame are required to rotate back to inertial frame. Components of angular velocity in Cartesian coordinates (Ω_x, Ω_y, Ω_z) are obtained as follows.

$$\begin{bmatrix} \Omega_x \\ \Omega_y \\ \Omega_z \end{bmatrix} = R_1R_2R_3R_4 \begin{bmatrix} \dot{\theta} \\ 0 \\ 0 \end{bmatrix} + R_1R_2R_3 \begin{bmatrix} 0 \\ 0 \\ \dot{\phi} \end{bmatrix} + R_1R_2 \begin{bmatrix} 0 \\ -\dot{\beta} \\ 0 \end{bmatrix} \tag{2.27}$$

Finally, cyclic motions are provided by UDF. Time dependent solver is ready to solve accurate motion. The shortened version of UDF is stated in Appendix A.

CHAPTER 3

RESULTS AND DISCUSSION

3.1 Hover Flight Cases

Hover flight cases are solved in a steady state manner with the MRF method as mentioned earlier. Three hovering rotors are analysed. The first one is known as Caradonna Tung rotor in literature [3]. The study made by Caradonna and Tung [3] includes hover cases with various collective angles and angular velocities. These important test series are benchmark for hovering cases. The case with a collective angle of 8 degrees is selected. The tip Mach number of the selected case is similar to that of TAI whirl tower case [15]. The RANS equations are solved in a steady state way. Chordwise pressure distributions at different spanwise sections are compared with experimental results. The second rotor is the TAI whirl tower rotor [15]. Eight different collective pitch angles are computed, from zero to 14 degrees with 2-degree interval. Rotor performance curves and sound pressure levels at a microphone location are compared with experimental study. The third rotor is the untwisted model of the UH-1H rotor which has symmetric NACA0012 airfoils. A non-lifting case (zero collective angle) with a transonic tip Mach number is considered [16]. Attained flow solutions of this rotor are used as input for computations of high speed impulsive noise. Computations of noise for both TAI whirl tower and UH-1H rotors are performed by the noise prediction code developed under a TAI/DKTM project [4]. Flow conditions and computation details of the hover cases are summarized in Table 3.1. During the simulations, under-relaxation factors control the update of computed flow variables at each iteration. The values of pseudo transient under-relaxation factors are stated in Table 3.2. Under-relaxation factor of temperature is valid for only invis-

Table 3.1: Summary of hover case simulations

	Caradonna and Tung	TAI whirl tower	UH-1H
Flow conditions			
M_{tip}	0.44	0.49	0.88
$\theta_{collective}$	8^o	0^o, 2^o, 4^o, 6^o, 8^o, 10^o, 12^o, 14^o	0^o
$\beta_{conning}$	0^o	2^o	0^o
Computation details			
Model	Viscous, Spalart Allmaras	Viscous, Spalart Allmaras	Inviscid
Solution domain	full rotor	full rotor	periodic
Number of cells	7,700,000	10,300,000	7,100,000
Number of surface grid on a blade	58,000	87,000	109,000
Length of edge of tet grid in refinement region	0.12c	0.12c	0.20c

Table 3.2: Pseudo transient under-relaxation factors

Pressure	Momentum	Density	Body forces	Energy	Temperature	Modified turbulent viscosity	Turbulent viscosity
0.4	0.4	1	1	0.75	0.75	0.75	1

cid case while modified turbulent viscosity and turbulent viscosity is relevant to only viscous flows.

3.1.1 Caradonna-Tung

For this rotor RANS solutions with Spalart-Allmaras one equation turbulence model are carried out in a steady state way. The rotor consists of two untwisted and symmetric (NACA0012) blades [3]. The radius of the rotor is 1.143 meters, and aspect ratio of the blades is 6. Experiments are run in a wide range of angular velocity (650 rpm to 2540 rpm), and collective angles (zero to 12 degree). A single case with an eight degree collective angle and 1250 rpm is analysed. This rotational velocity is examined because the tip Mach number is 0.44 which is same as TAI whirl tower [15] discussed in the next section. Also, Reynolds number is same as TAI whirl

tower. When tip velocity is considered, Reynolds number is approximately equal to 1.9×10^6. Characteristic length is chord in the calculations of Reynolds number. The distances between rotation center and the outer boundaries on the side and top are about 10 rotor radii. The bottom boundary is away from the rotor center by 15 rotor radii. Mesh refinement is performed in the regions of high flow gradients, such as near tip vortex flow paths. The edge of the largest tetrahedron mesh in the refined region is defined as 0.12 chord. Figure 3.1 shows some different views of the solution domain which is made of cylindrical shape and the mesh refinement regions. Mesh study is carried out in order to demonstrate that solution is independent of number of cells. For relatively coarse mesh including 6.1 million cells, the edge of the largest tetrahedron mesh in the refined region is equal to 0.18 chord. Figure 3.3 indicates pressure distributions at the tip regions. There is no important difference between the solutions obtained on two grids. Figure 3.2 illustrates the pressure distributions along chord at five different spanwise sections for finer mesh. Pressure coefficient distribution at a section of blade is obtained by using the velocity normal to that section of blade. It seems that the pressure values on upper surfaces are slightly overestimated at the leading edge. Nevertheless, a good overall agreement between the experimental data and the computed results is observed.

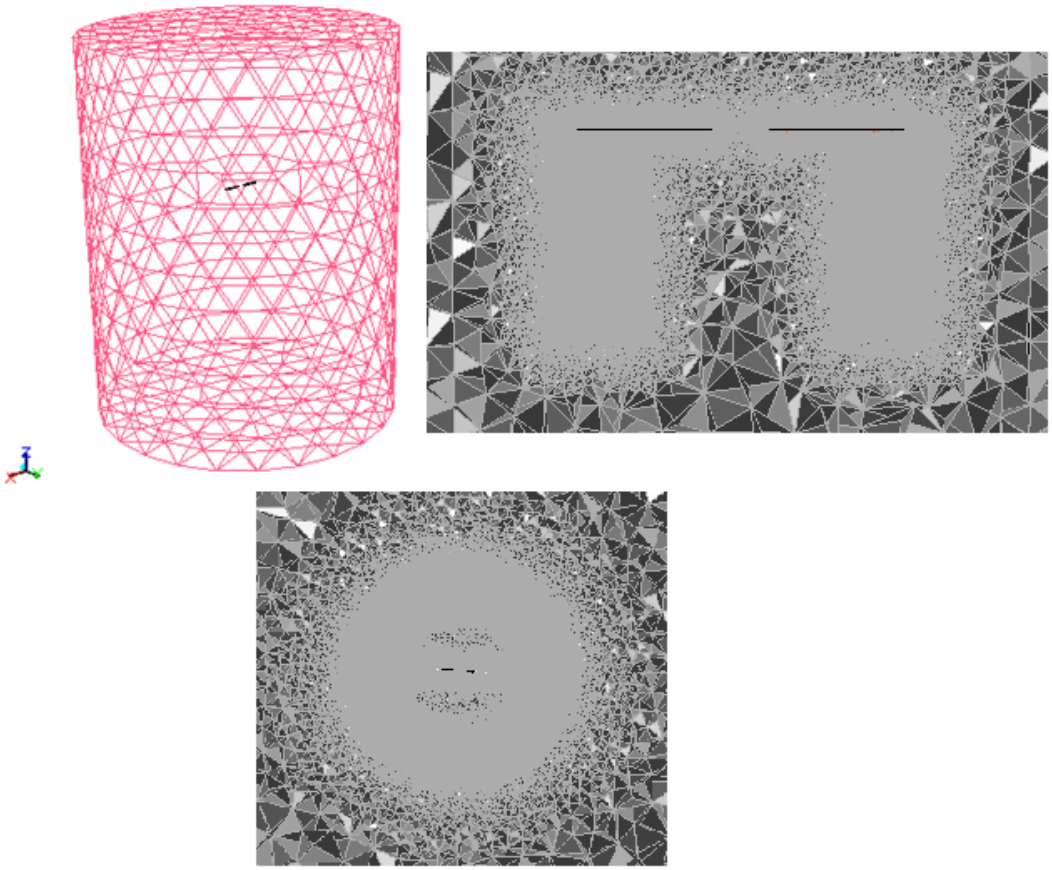

Figure 3.1: Solution domain and mesh refinement regions

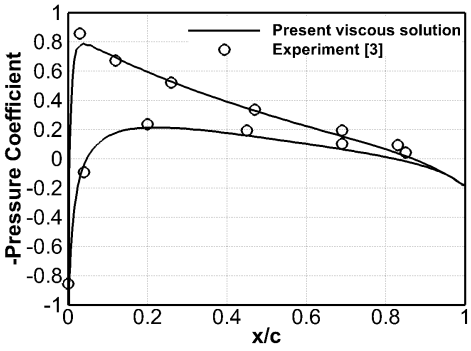

(a) r/R=0.50

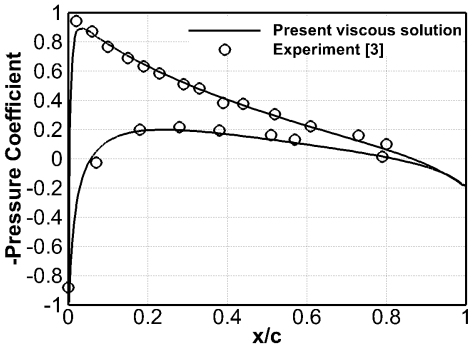

(b) r/R=0.68

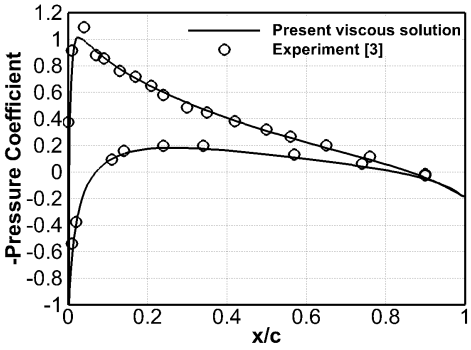

(c) r/R=0.80

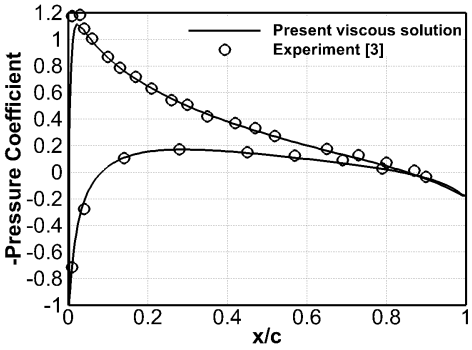

(d) r/R=0.89

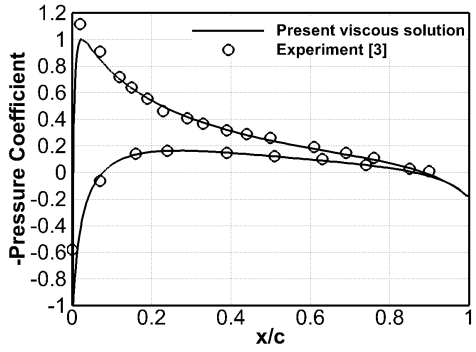

(e) r/R=0.96

Figure 3.2: Pressure distribution comparison for the Caradonna and Tung case [3]

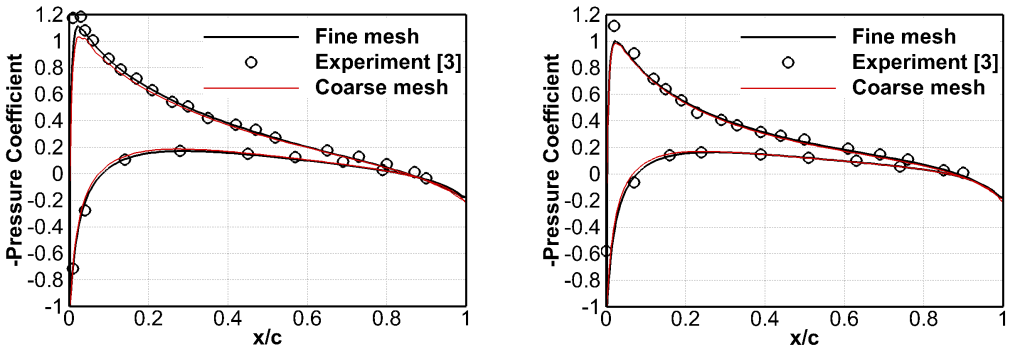

(a) r/R=0.89

(b) r/R=0.96

Figure 3.3: Pressure distribution comparison between coarse and fine meshes for the Caradonna and Tung case [3]

3.1.2 TAI Whirl Tower

The method used in the solution of Caradonna and Tung [3] rotor is discussed in the preceding section. This method is applied to the 3-meter radius experimental rotor which is designed by TAI. The RANS equations are solved with Spalart-Allmaras one equation turbulence model. Meshing strategy is also similar to that of hovering Caradonna and Tung [3] rotor. The first cell wall y^+ value is set nearly equal to a minimum value of 1, which is in the vicinity of blade tip. As mentioned before, eight simulations are carried out from zero to 14 degree collective pitch angles with an interval of 2 degrees. Double precision arithmetic is used in simulations in order to minimize round-off error. Also, convergence plays a crucial role to attain reliable CFD results. Iterations for steady state solution are continued until about a five orders of magnitude residual reduction.

Monitoring the values of the produced thrust and torque during the solution is also a good way of observing the convergence. This is shown in Figure 3.4. Figure 3.5 illustrates velocity magnitude contours on a vertically sliced plane through the rotor center as well as gage pressure contours on a blade. Qualitatively, no abnormalities such as discontinuities in gage pressure or velocity contours are observed in compu-

Table 3.3: Normalization variables of TAI whirl tower case

Chord $[m]$	Density $[kg/m^3]$	Rotor radius $[m]$	Rotor Area $[m^2]$	Angular velocity $[rad/s]$	Number of blades	Solidity
0.1778	1.0584	2.97	27.7117	56.5487	2	0.0381

tations of rotor flow fields. In order to compare the obtained computational results with the measured thrust and torque values, a normalization was performed for thrust and torque values. Namely, the thrust and torque coefficients are obtained. Table 3.3 illustrates the geometric properties and operational conditions used in normalization.

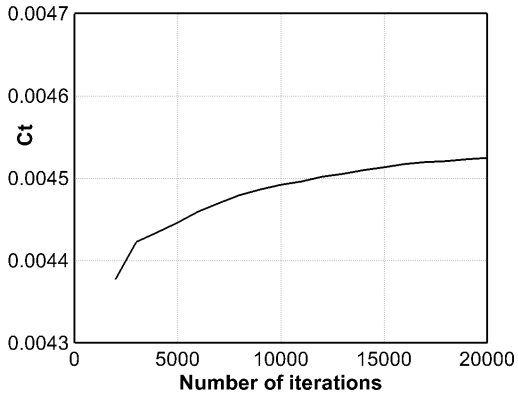

(a) $\theta = 10^o$

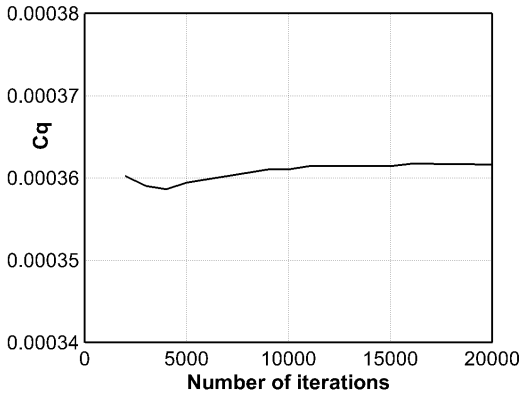

(b) $\theta = 10^o$

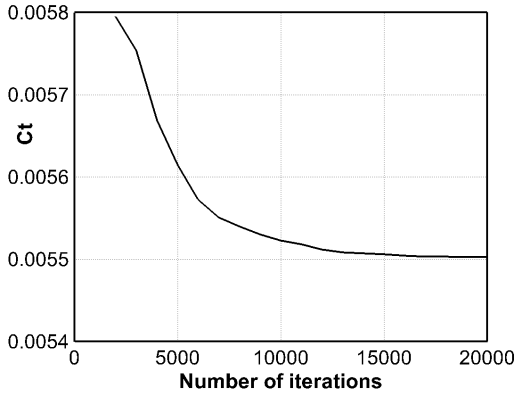

(c) $\theta = 12^o$

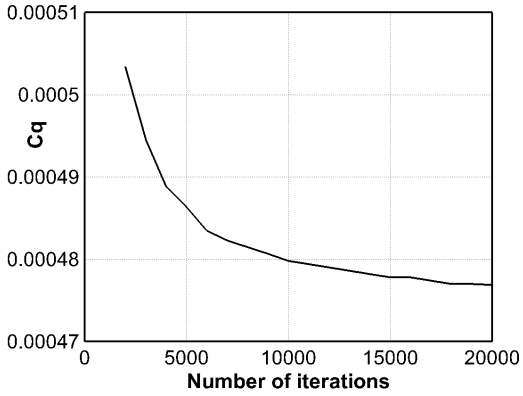

(d) $\theta = 12^o$

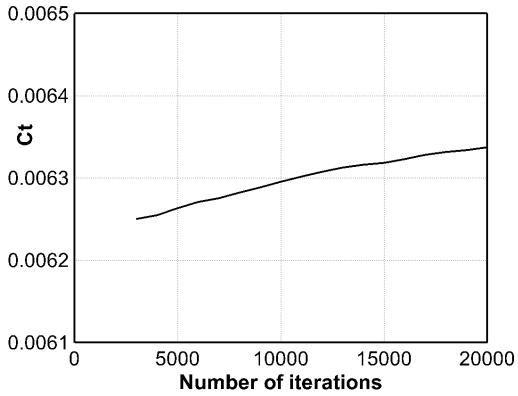

(e) $\theta = 14^o$

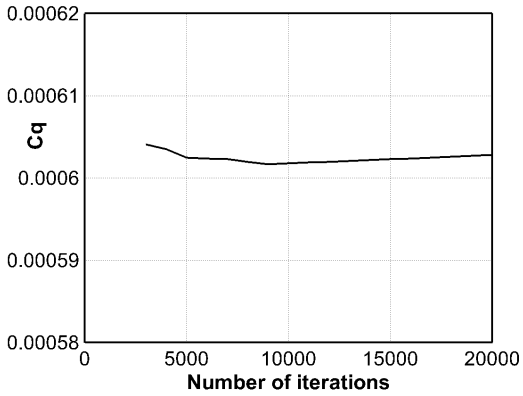

(f) $\theta = 14^o$

Figure 3.4: TAI whirl tower convergence history

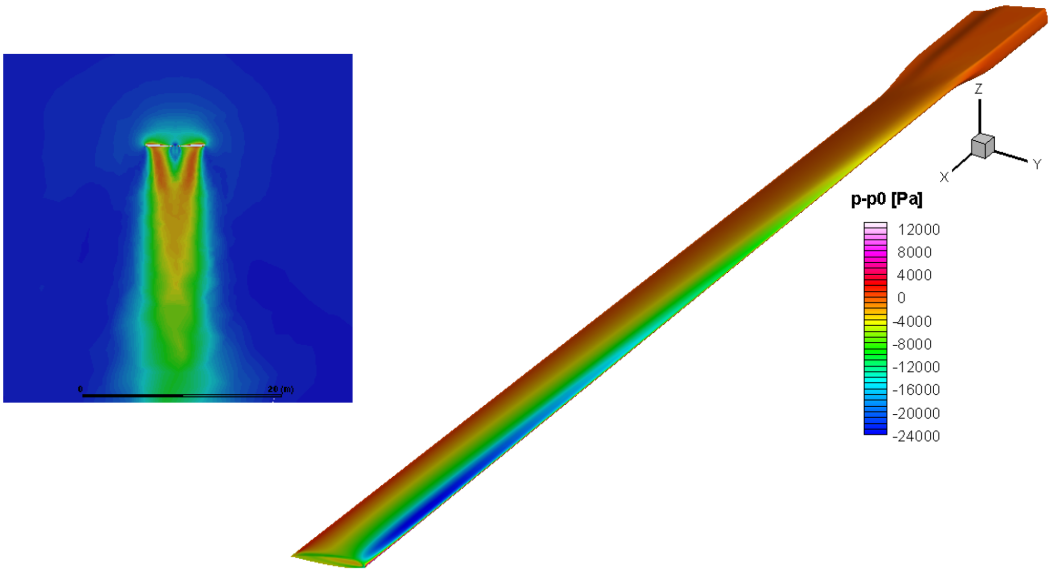

Figure 3.5: TAI whirl tower downwash and gage pressure contour at $\theta = 12^o$

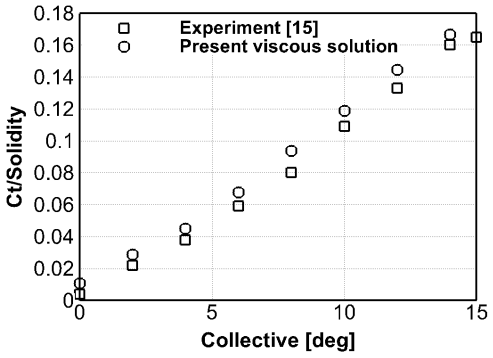

(a) thrust vs. collective

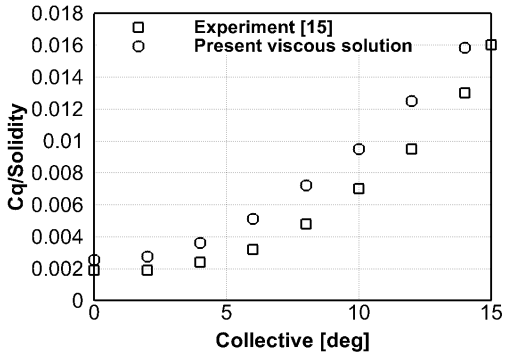

(b) torque vs. collective

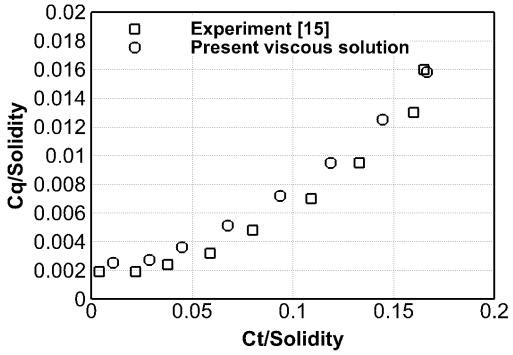

(c) torque vs. thrust

Figure 3.6: Comparisons of present viscous solutions with tested non-dimensional thrust and torque values for TAI whirl tower cases

Non-dimensional values of the thrust and torque are compared with the experiment results [15] in Figure 3.6. The predictions of thrust coefficient for different collective angles show generally good agreement with experimental data. The variation of the torque coefficient with collective angles has similar trend with experiment. However, a nearly 25 percent difference between the attained results and experimental data can be detected at some collective angles. It is known that thrust and torque are related to lift and drag, respectively. Hence, it is expected that the thrust is predicted generally more accurately than the torque. On the other hand, a significant performance curve which is the change of non-dimensional thrust with non-dimensional torque agrees

well with the experimental data. This curve is important because it compares the performance of actual rotor with the performance of an ideal rotor like figure of merit [7].

Figure 3.7 illustrates the chordwise pressure coefficent variations at different spanwise sections for collective angles of 4, 8 and 12 degrees. These type distributions were used as input into noise prediction code developed in TAI [4]. The noise prediction code [4] uses the flow variables such as static temperature, static pressure, density, velocity components. This noise prediction algorithm is based on integration of the Ffowcs William-Hawkings equation. Figure 3.8 shows the comparisons of sound pressure levels of the experiment and code at a microphone location. While blue bars represent acoustic calculations without ground reflection, orange bars illustrate results with inclusion of ground reflection for acoustic calculations. Attained results show very good agreement with experiment for the first two harmonics. Capturing similar accuracy for the higher harmonics requires using of finer meshes, because higher harmonics are results of mainly multiple effects of trailing tip vortices.

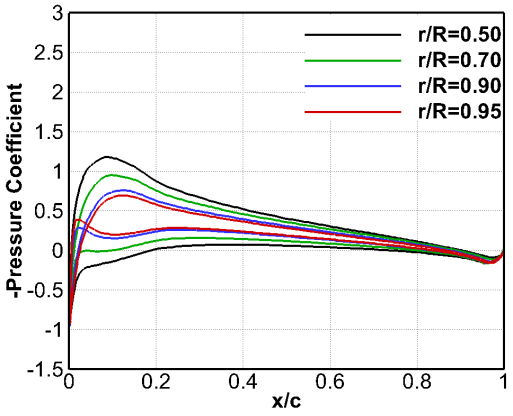

(a) $\theta_{collective} = 4^o$

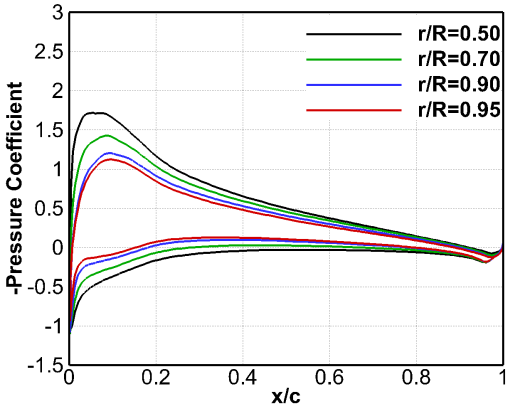

(b) $\theta_{collective} = 8^o$

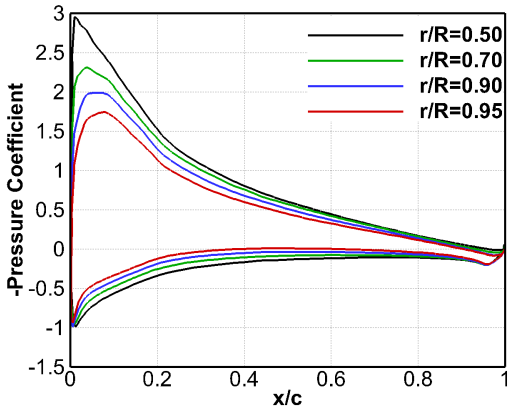

(c) $\theta_{collective} = 12^o$

Figure 3.7: Pressure distributions of TAI whirl tower rotor blade

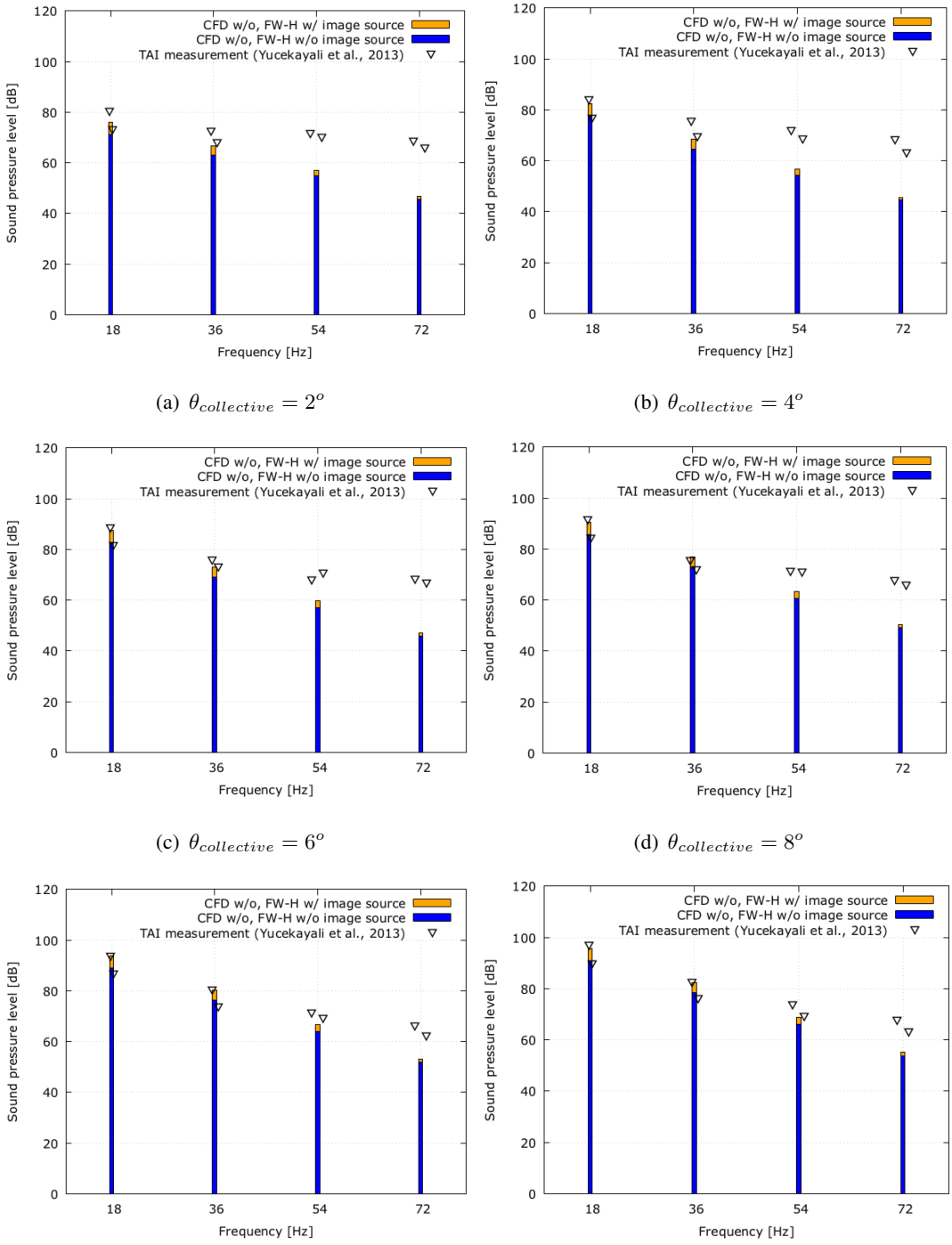

(a) $\theta_{collective} = 2^o$

(b) $\theta_{collective} = 4^o$

(c) $\theta_{collective} = 6^o$

(d) $\theta_{collective} = 8^o$

(e) $\theta_{collective} = 10^o$

(f) $\theta_{collective} = 12^o$

Figure 3.8: Comparisons of acoustic predictions of TAI whirl tower rotor with experimental data [4]

3.1.3 UH-1H with Transonic Flight Conditions

Solutions of Euler equations in steady state manner are carried out in this section. The discretization of the equations are similar to those given in Sections 3.1.1, and 3.1.2. However, some of the boundary conditions are naturally different than the above hover cases. Firstly, inviscid wall boundary condition is applied on the blade surfaces . Secondly, solution is not carried out for 360-degree domain, rather on half of it with periodic boundary conditions. Domain boundaries are indicated in Figure 3.9.

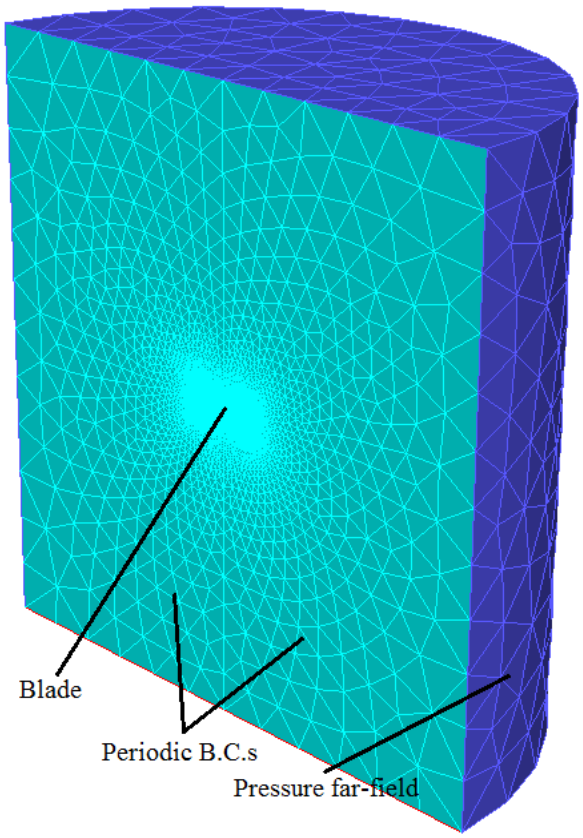

Figure 3.9: Domain boundaries of UH-1H rotor

Also, flight conditions of UH-1H rotor are different from the previous hover cases. The first difference is transonic tip Mach number ($M_{tip} = 0.88$). The second one is rotor blade is symmetric and untwisted. Hence, thrust generation does not exist. Because of these two reasons, mesh refinement region also includes some differences. Shock waves and supersonic flow regions occur both below and above blade tip, and

they extend out beyond the rotating blade tip. Mesh refinement focuses in these regions.

Figure 3.10 indicates the computed pressure coefficients along chord at different wingspan sections. Pressure discontinuity near tip region ($r/R = 0.95$) demonstrates that a shock wave exists there. The same pressure distribution on upper and lower surfaces means there is no thrust generation. Figure 3.11 shows the static pressure and relative Mach number contour lines near the tip on the rotor plane. Relative Mach number contour lines illustrate the sonic cylinder, and shock wave around tip region. In general, as tip Mach number is between 0.8 and 0.9, weak shock waves take place in tip region. When tip Mach number is greater than about 0.9, the shocks become delocalized, extending beyond the blade tip. This causes intense and high frequency noise in directions near the plane of rotor [20]. Therefore, shock delocalization arises when the tip Mach number reaches a critical value about 0.9. At this Mach number, the transonic zone and shock waves expand radially. Shock waves detach from the blade tip, and then they reach the sonic cylinder. The flow discontinuity on the sonic cylinder causes a weak acoustic shock in the far field. The earlier works proposed that tip Mach number starting the shock delocalization for untwisted and symmetric UH-1H rotor was between 0.88 and 0.90 [16]. Tip Mach number of 0.88 seems very close to beginning of shock delocalization. Therefore, accurate solution of the flow field is essential to predict high speed impulsive noise.

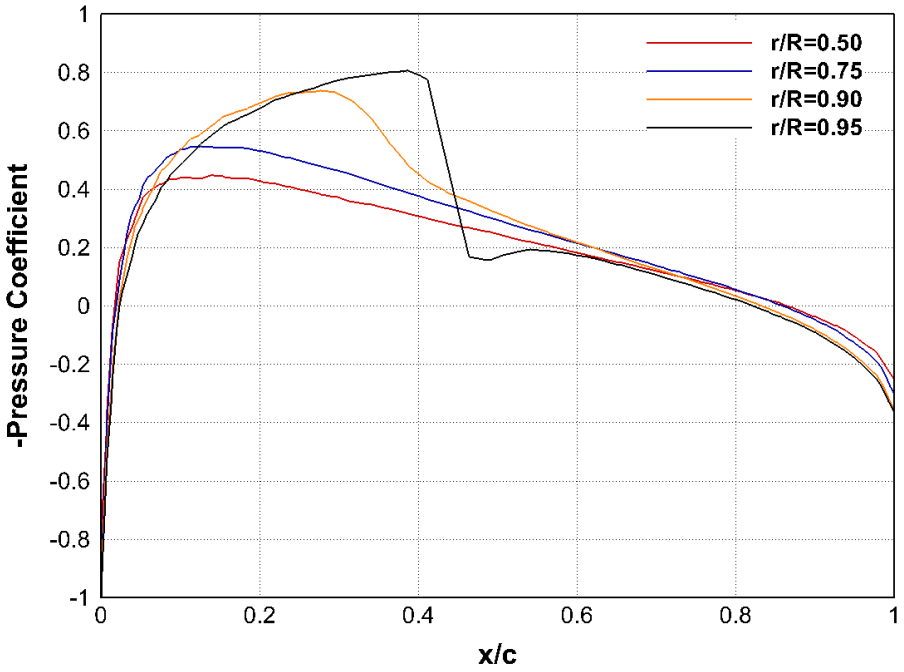

Figure 3.10: Pressure coefficient distribution along chord at different spanwise sections for UH-1H case

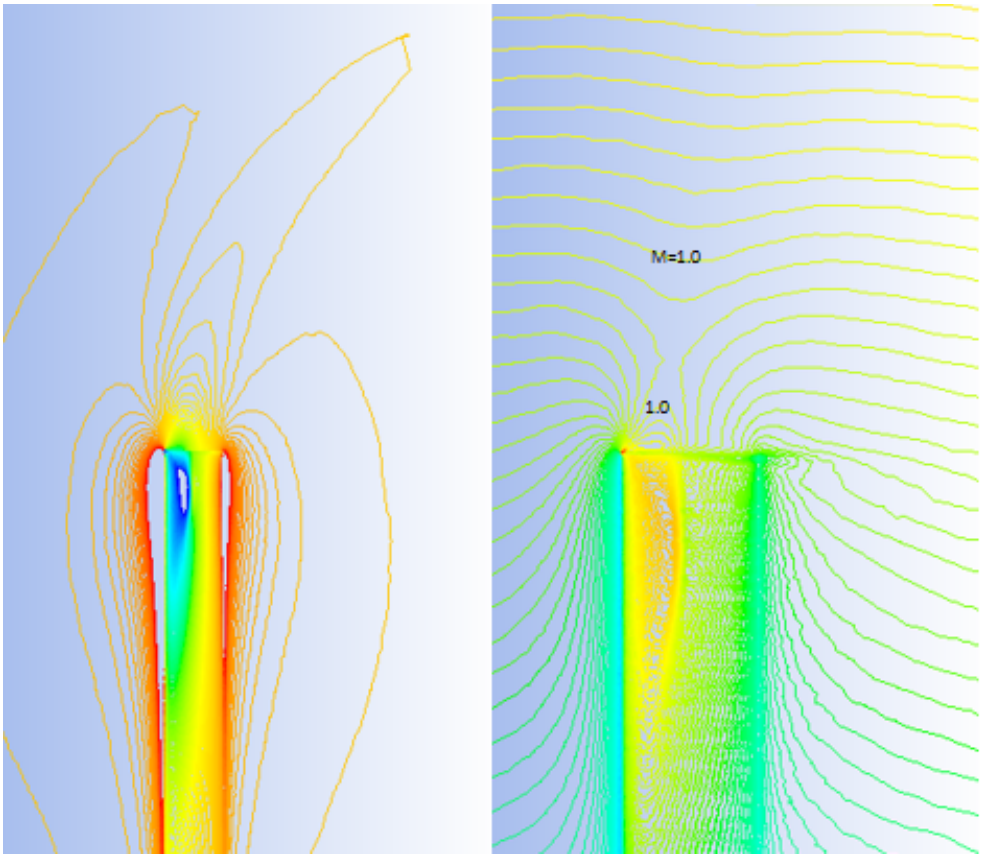

Figure 3.11: Static pressure (left) and relative Mach number (right) on UH-1H rotor plane (top view)

3.2 Forward Flight Cases

In this section, flow solutions of helicopter rotors in forward flight are performed. Solutions of RANS equations are carried out in time-dependent manner. Third order MUSCL discretization is used in space, while first order implicit transient formulation is applied with pseudo subiterations. A number of 15 subiterations are forced in aim of approximately 4 orders of magnitude residual reduction at each physical time step. The physical time step is chosen such that it corresponds to a 0.25 degree of rotor rotation. Due to transient nature of the solutions, a mesh motion is realized between two consecutive time steps.

Two forward flight cases are considered. The first one, discussed in detail in Section 3.2.1, does not include cyclic blade motions. Hence, only grid rotation about the

Table 3.4: Summary of forward flight case simulations

	Onera two-bladed	Caradonna and Tung
Flow conditions		
$M_{hovertip}$	0.605	0.60
Advance ratio	0.55	0.25
Cyclic motions of blade	not exist	exist
Computation details		
Model	Viscous, Spalart-Allmaras	Viscous, Spalart-Allmaras
Solution domain	full rotor	full rotor
Number of cells	4,500,000	6,600,000
Number of surface grid on a blade	30,000	49,000
Length of edge of tet grid in refinement region	0.15c	0.15c
Number of revolutions	4	4
Number of cores	32	32
Simulation time [h]	70	84

rotation axes is sufficient to simulate the physics of the problem. This flight condition is solved in preparation for the next case that includes cyclic motion. Due to cyclic motion, the latter case is the more challenging one. It is solved through mesh motion and deformation which are provided during the transient solution through the UDF capability of the solver. Details are given in Section 2.5. Table 3.4 gives a summary of the flow conditions, and computational details for both forward flight cases.

3.2.1 Onera Two-bladed Model Rotor without Periodic Motions of Blade

One of the major objectives of the thesis is to solve flow field of helicopter rotors in forward flight with cyclic motions accurately. For this purpose, forward flight without cyclic motion case is initially performed in order to get ready for cyclic motion case. Figure 3.12 specifies the geometric properties of Onera two-bladed model rotor solved. The length of the root chord is 0.166 meters, while radius of the rotor is 0.75 meters. The profile relative thickness decreases linearly from 17 percent at 0.37R to 14.5 percent at 0.8R, then down to 9 percent at the tip.

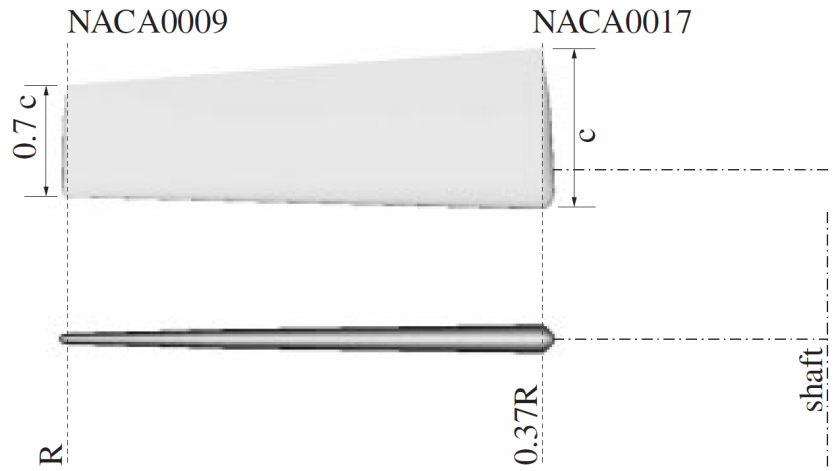

Figure 3.12: Geometric specifications of Onera model rotor blade[5]

The advance ratio for the rotor is 0.55, and forward flight Mach number is 0.33275. Therefore, rotor is exposed to transonic flow at advancing side. When advancing tip velocity is considered, Reynolds number approximately equals to 2.1×10^6. In this case, unsteady RANS equations are solved. Figure 3.13 shows the comparisons of the attained results with the experimental study [6]. Pressure distributions at azimuth angles of 60^o and 120^o degrees are extracted after three revolutions of rotor are completed. The major challenge in this case is to capture the shock formation and pressure discontinuity accurately. Figure 3.13 indicates good agreement between the computed and tested surface pressure distributions.

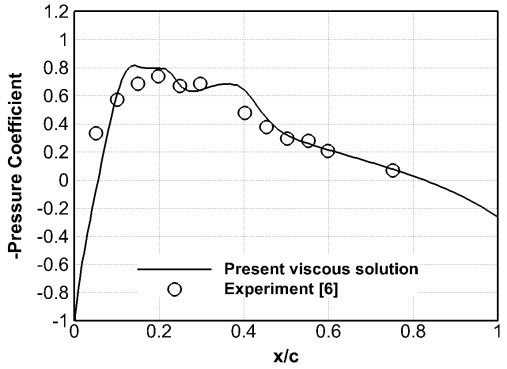

(a) $\psi = 60^o, r/R = 0.891$

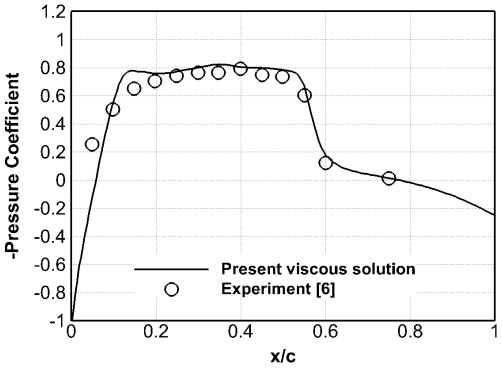

(b) $\psi = 120^o, r/R = 0.891$

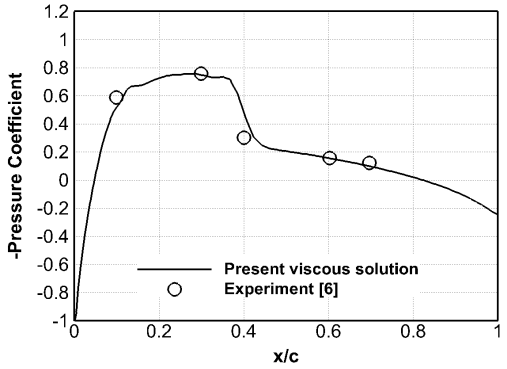

(c) $\psi = 60^o, r/R = 0.946$

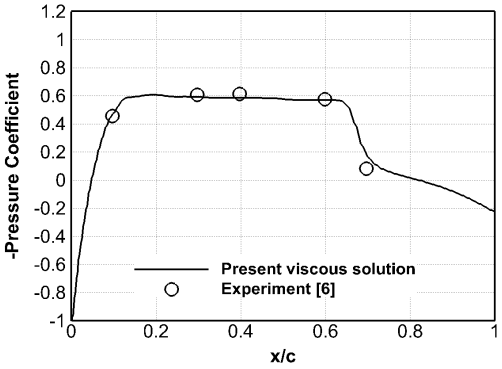

(d) $\psi = 120^o, r/R = 0.946$

Figure 3.13: Pressure distribution comparison between experiment [6] and present viscous solution for Onera two-bladed model rotor

3.2.2 Caradonna-Tung with Periodic Motions of Blade

In this section, solutions of the RANS equations with one equation Spalart-Allmaras turbulence model are carried out in a totally time dependent manner. No-slip wall boundary condition on the blade surfaces, and pressure far-field boundary condition at the far field boundaries are applied. Figure 3.14 illustrates the solution domain, and regions of mesh refinement in various views. Third order MUSCL discretization is employed in space. On the other hand, first order implicit transient formulation strategy is applied with a number of subiterations which aim at four orders of magnitude residual reduction at each time step.

Forward flight Mach number of Caradonna and Tung rotor with two blades is equal to 0.15, and the advance ratio is 0.25. When advancing tip velocity is considered, Reynolds number approximately equals to 3.3×10^6. The Parameters of the prescribed cyclic motions of pitching, flapping, and lead-lag angles are given in Table 3.5. Before comparison of the present viscous solution with numerical results from literature [5], given cyclic motions to the blades, that is kinematics of blades are checked. Analytically calculated kinematic motion is compared with that numerically calculated one through the written UDF module. Guidance on how to provide calculated kinematic motion both analytically and numerically is presented in Section 2.5. For this purpose, a point located at the trailing edge of the tip of a blade is exposed to analytical and numerical periodic motions. Figure 3.15 indicates the difference between the numerically and analytically obtained maximum deflections of this point in the rotor axis direction due to cyclic motion. Difference over greatest deflection is around 0.006 for some azimuthal positions. In other words, the distance between blades exposed to analytical and numerical motion is about 0.5mm that is good agreement. Thus, it can be stated that present solution provides accurate cyclic motions and rotation.

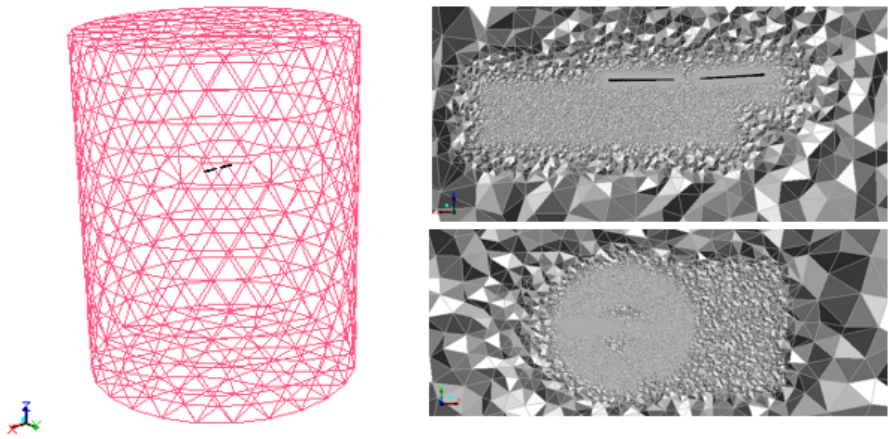

Figure 3.14: Solution domain and mesh refinement regions for forward flight cases

Table 3.5: Prescribed cyclic motions of blade for forward flight with cyclic motion case

θ_0	θ_{1s}	θ_{1c}	β_0	β_{1s}	β_{1c}	ϕ_0	ϕ_{1s}	ϕ_{1c}
4.0^o	2.0^o	0.0^o	1.5^o	2.0^o	2.0^o	0.0^o	-2.0^o	0.0^o

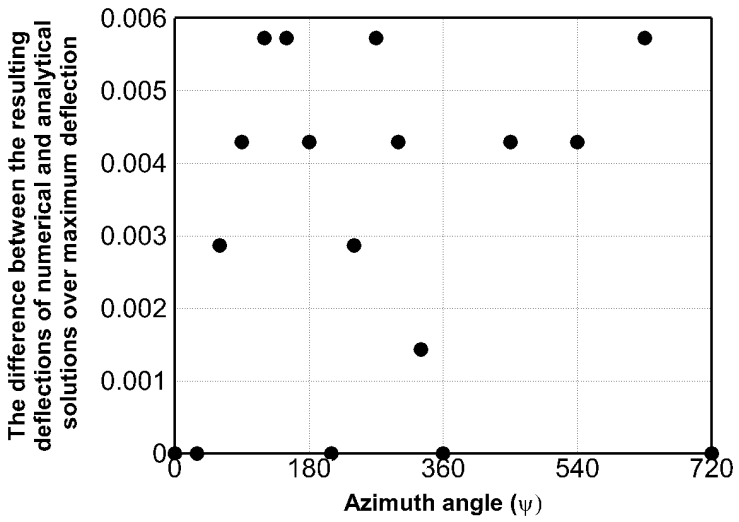

Figure 3.15: Comparison of analytical and numerical cyclic motions for forward flight with cyclic motion case

During the solution, forces produced by the rotor in upward direction $(+z)$ and in flow direction $(+x)$ are normalized, and represented by symbols C_z, and C_x, respectively. Figure 3.16 indicates the normalized forces during last two rotations. Because rotor has two blades, periodic oscillations with an interval of 180 degrees are expected. It is clearly seen the periodic oscillations during last two rotations, forth and fifth one. Pressure distributions are captured during the last rotation, fifth one. Qualitatively, Figure 3.17 shows the pressure contours on a blade at azimuth angles of $30^o, 90^o, 150^o, 210^o, 270^o, 330^o$. Quantitatively, pressure distributions along the chord at spanwise section of $r/R = 0.89$ for different azimuthal positions are obtained. Attained results are compared with the numerical analysis of [5]. Although the lift of the rotating blade is little overestimated for all azimuthal positions, Figure 3.18 shows good agreement between the present viscous solution and available numerical solution [5].

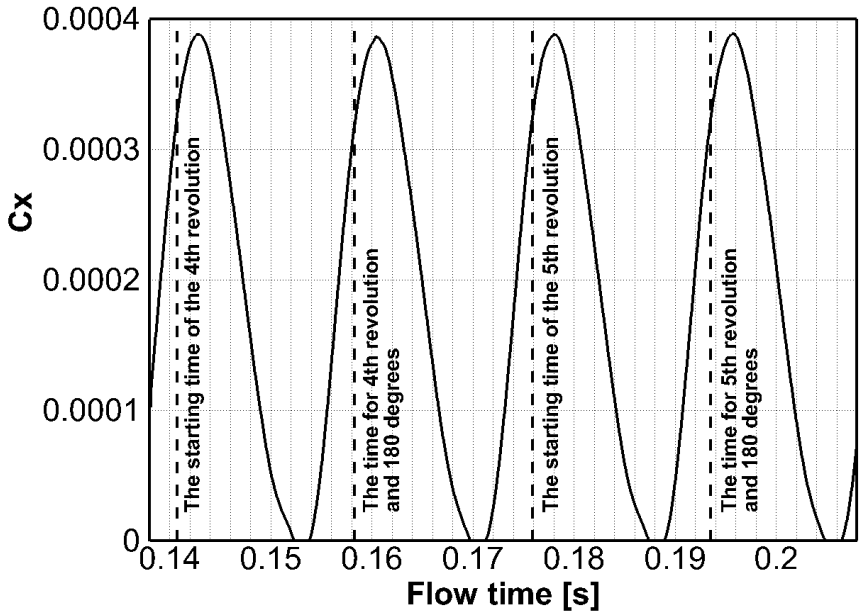

(a) Normalized force in flow direction vs. time

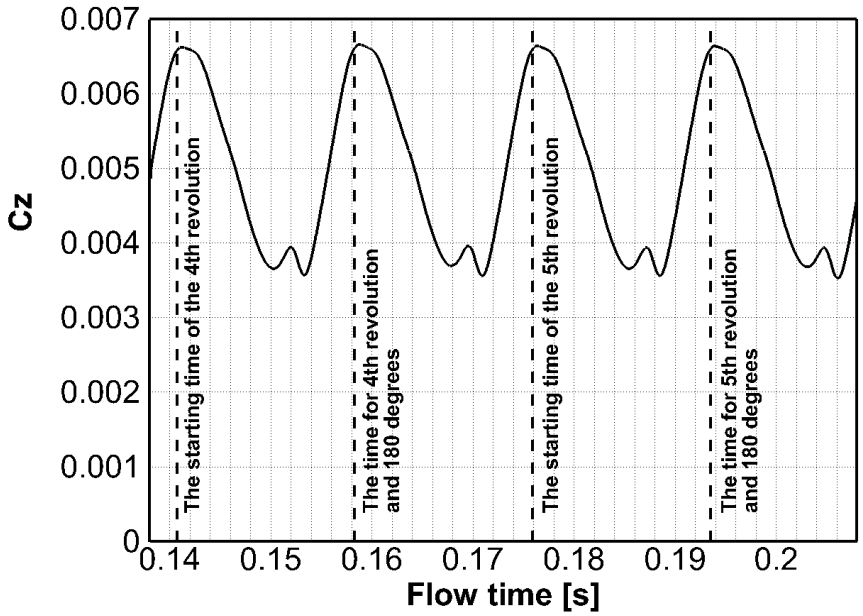

(b) Normalized force in upward direction vs. time

Figure 3.16: Normalized forces on Caradonna and Tung rotor in forward flight during 4th and 5th revolutions

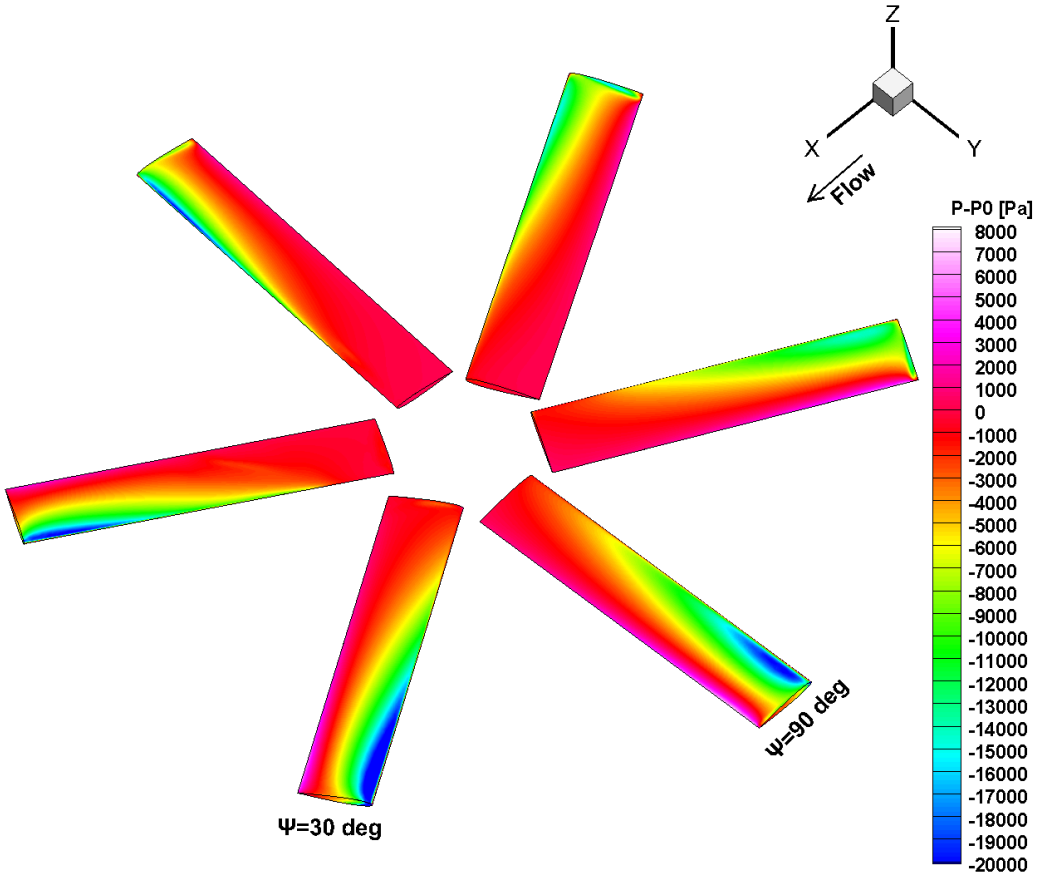

Figure 3.17: Pressure contours of a blade for various azimuthal positions for forward flight with cyclic motion case

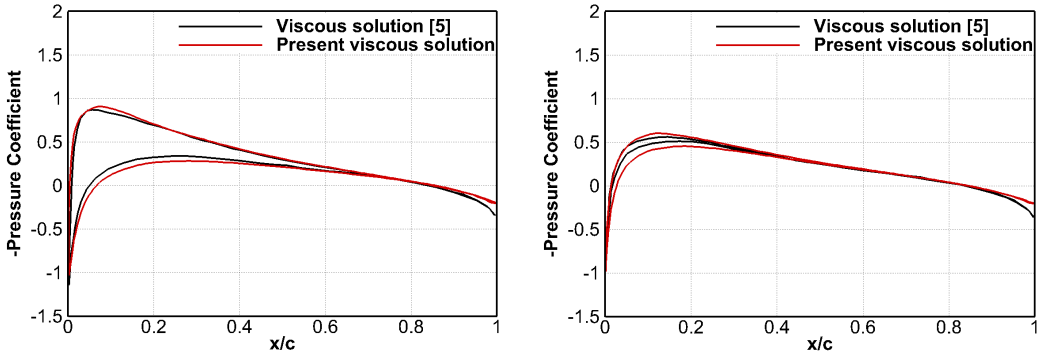

(a) $\psi = 30^o$

(b) $\psi = 90^o$

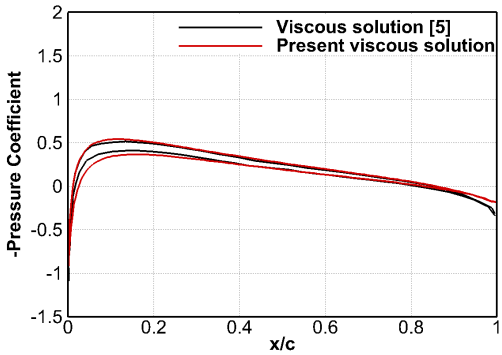

(c) $\psi = 150^o$

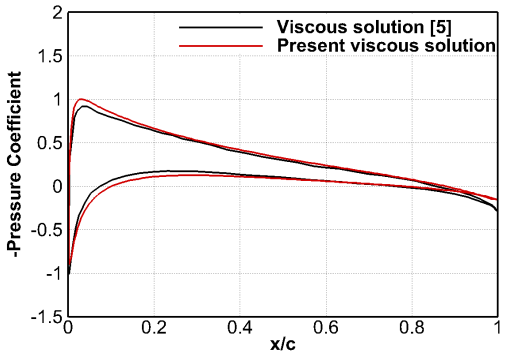

(d) $\psi = 210^o$

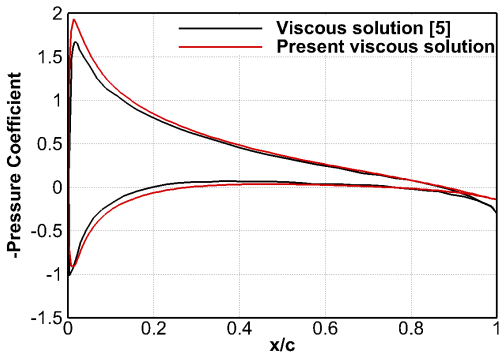

(e) $\psi = 270^o$

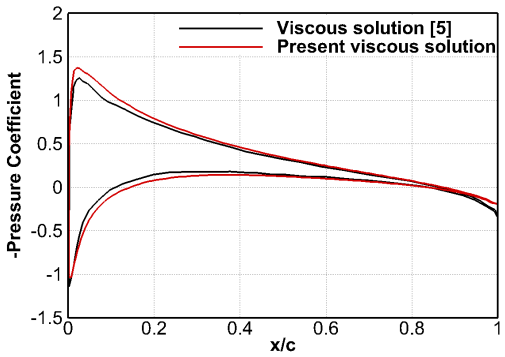

(f) $\psi = 330^o$

Figure 3.18: Pressure distribution comparison for forward flight with cyclic motion case [5]

CHAPTER 4

CONCLUSION

In this thesis, flow solutions of helicopter rotors in hover and forward flight have been carried out. Hover cases have been simulated in steady-state manner, while forward flight cases have been analysed in time-dependent manner due to cyclic blade motions. Both solutions of Euler and Reynolds-Averaged Navier-Stokes (RANS) equations have been performed. While Euler equations are usually sufficient to represent the rotor aerodynamics in the cases of high Reynolds numbers, RANS equations are needed to be solved in cases of turbulence and viscous effects being relatively significant.

In the introductory chapter of the thesis, fundamentals of helicopter rotor aerodynamics, and the additional complexity involved in forward flight cases are briefly discussed. Also, the CFD modelling approaches used in literature are reviewed briefly. In the second chapter, the solution strategies are expressed with a description of the commercial solver, Ansys Fluent employed. The governing equations of the hover cases are given by writing them with respect to rotating frame. On the other hand, in forward flight analysis, unsteady flow solutions are carried out by first order implicit transient formulation. Forward flight without cyclic motions are figured out by rotating the computational mesh. However, forward flight with cyclic motions requires a different approach. The user defined function (UDF) capacity of Fluent is employed to give mesh motions, specifically blade cyclic, flapping and lead-lag motions. In this approach, both the blade surface mesh and the boundary layer mesh are moved together as a rigid object through a UDF module written for this purpose, while the mesh elements adjacent to the boundary layer are deformed in order to avoid mesh

overlapping due to lead-lag and flapping. Two critical issues related to the mesh motion are time step size and mesh deformation itself. The previous one is important because rigid motion is performed numerically by integration of angular velocity. Hence, time step size must be small enough to obtain accurate motion. The latter one is significant because mesh deformation should take place adjacent to boundary layer, instead of blade in order to obtain stable pressure distributions.

Three hover and two forward flight cases are solved. Viscous solutions of Caradonna and Tung [3] rotor, and Turkish Aerospace Industries (TAI) whirl tower rotor [15] with subsonic tip Mach numbers are carried out by considering the whole rotor. While inviscid solutions of UH-1H rotor with transonic flight conditions are performed by employing periodic boundary conditions. Pressure distributions and performance curves are compared with experimental data. Although it seems that torque values are little overestimated, overall the agreement with experimental data is good for pressure distributions, thrust values, and figure of merit. Also, CFD data are used as input into a noise prediction code developed under TAI Rotary Wing Technology Center [4]. Sound pressure levels and high speed impulsive noise are obtained for the hover cases with subsonic and transonic tip Mach number, respectively. Sound pressure level comparisons with TAI whirl tower measurements are quite well for the major frequency and its first harmonic. However, some differences exist at higher harmonics which could be due to insufficient resolution.

Onera two-bladed model rotor [6] without cyclic motions is also solved. The rotor blades have transonic tip Mach number on the advancing side. Unsteady, viscous solutions are carried out. Pressure distributions are compared with the available experimental data at various azimuthal positions. General trends of pressure distributions are promising. Forward flight analysis of Caradonna and Tung rotor with cyclic motions is relatively more challenging than the others because of the mesh deformation and cyclic blade motions. For this case unsteady RANS solutions are carried out. Attained results are compared with the numerical solution of [5]. Although lift of the rotating blade is slightly overestimated for all azimuthal positions, attained viscous solution indicates good agreement in general, with the numerical viscous solution of [5].

4.1 Future Works

- Structured multi-block topology can be constructed. Comparisons between present unstructured meshes approach with structured multi-block topology could be carried out.
- Chimera (Overset) method [21] including blade-fixed grids and background mesh can be conducted. Comparisons of present mesh deformation approach and Chimera method could be carried out.
- Aeroelastic effects can be taken into account by coupling the flow solver with a finite element model of the blade.
- Coupling of the flow solver with a rotor trimming approach can be implemented.

REFERENCES

[1] J. G. Leishmann. *Principles of Helicopter Aerodynamics*. Cambridge University Press, second edition, 2006.

[2] J. Seddon. *Basic Helicopter Aerodynamics*. BSP Professional Books, first edition, 1990.

[3] F. X. Caradonna and C. Tung. Experimental and Analytical Studies of a Model Helicopter Rotor in Hover. Technical report, NASA, 1981.

[4] Y. Özyörük, A. Ünal, and A. O. Yüksel. Noise predictions of helicopter rotors in hover and forward flight. In *23rd AIAA/CEAS Aeroacoustics Conference*, Denver, 2017.

[5] R. Steijl, G. Barakos, and K. Badcock. A Framework for CFD Analysis of Helicopter Rotors in Hover and Forward flight. *International Journal for Numerical Methods in Fluids*, (January 2005):819–847, 2006.

[6] J-J. Philippe and J-J. Chattot. Experimental and Theoretical Studies on Helicopter Blade Tips at ONERA. In *Sixth European Rotorcraft and Powered Lift Aircraft Forum*, Bristol, 1980.

[7] W. Johnson. *Rotorcraft Aeromechanics*. Cambridge University Press, 2013.

[8] J. N. Abras, C. E. Lynch, and M. J. Smith. Advances in Rotorcraft Simulations with Unstructured CFD. In *AHS 63rd Annual Forum*, Virginia Beach, VA, 2007.

[9] K. S. Brentner and F. Farassat. Modeling aerodynamically generated sound of helicopter rotors. *Progress in Aerospace Sciences*, 39(2-3):83–120, 2003.

[10] F. X. Caradonna. The Application of CFD to Rotary Wing Aircraft. Technical Report 102803, NASA, 1992.

[11] Y. R. Ganti. CFD Analysis of a Slatted UH-60 Rotor in Hover, 2012.

[12] G. R. Srinivasan and J. D. Baeder. TURNS: A Free-Wake Euler/Navier- Stokes Numerical Method for Helicopter Rotors. *AIAA Journal*, 31(5):959–962, 1993.

[13] R. E. Brown. Rotor Wake Modeling for Flight Dynamic Simulation of Helicopters Introduction. *AIAA Journal*, 38(1), 2000.

[14] G. R. Srinivasan and W. J. McCroskey. Navier-Stokes Calculations of Hovering Rotor Flowfields. In *AIAA Atmospheric Flight Mechanics Conference*, Monterey, CA, 1987.

[15] A. Yücekayalı, A. Ezertaş, and Y. Ortakaya. Whirl Tower Testing and Hover Performance Evaluation of a 3 Meter Radius Rotor Design. In *7. AIAC*, Ankara, 2013.

[16] A. S. Morgans, S. A. Karabasov, A. P. Dowling, and T. P. Hynes. Transonic Helicopter Noise. *AIAA Journal*, 43(7):1514–1520, 2005.

[17] Ö. Yalçın. Development of a High Order Navier-Stokes Solver for Aeroacoustic Predictions of Wind Turbine Blade Sections, 2015.

[18] Ansys Academic Research Release 17.0. Customization Manuel. Technical report, 2017.

[19] M. Keating. Accelerating CFD Solutions. Technical report, 2011.

[20] M. S. Howe. *Acoustics of Fluid-Structure Interactions*. Cambridge University Press, 1998.

[21] H. Pomin and S. Wagner. Navier–Stokes Analysis of Helicopter Rotor Aerodynamics in Hover and Forward Flight. *Journal of Aircraft*, 39(5), 2002.

APPENDIX A

USER DEFINED FUNCTION

```
/*********************************************************
 * node motion about helicopter rotor blades
 * compiled UDF
 * written by Ali Oguz Yuksel & Yusuf Ozyoruk
 * Aerospace Eng. METU, Ankara, Sept. 2016
 * ********************************************************/
#include "udf.h"
#include "math.h"
#include "dynamesh_tools.h"

DEFINE_CG_MOTION(blade1, dt, vel, omega, time, dtime)
{
  real angvel, psi, theta, beta, lag, th0, bt0, lg0, thetadat,
      betadat, lagdat;
  real th1c, th1s, bt1c, bt1s, lg1c, lg1s, phase, ib, Nblades;
  /*** reset velocities ***/
  NV_S (vel, =, 0.0);
  NV_S (omega, =, 0.0);
  th0 = 4.0*M_PI/180; bt0 = 1.5*M_PI/180; lg0 = 0.0*M_PI/180;
  th1c = 0.0*M_PI/180; th1s = -2.0*M_PI/180;
  bt1c = -2.0*M_PI/180; bt1s = -2.0*M_PI/180;
  lg1c = 0.0*M_PI/180; lg1s = 2.0*M_PI/180;
  /*** lag positive when it has same direction with rotation ***/

  /** With respect to Steijl et. al.
  theta = th0 - th1c*cos(psi) - th1s*sin(psi);
  beta = bt0 - bt1c*cos(psi) - bt1s*sin(psi);
```

```
27  lag = lg0 - lg1c*cos(psi) - lg1s*sin(psi);  **/
28
29  /*** Thus, values of th1c, th1s, bt1c, bt1s, lg1c, lg1s are
        multiplied by mines sign (-) ***/
30
31  angvel = 178.5691; ib = 1.0; Nblades = 2.0;
32  phase = 2.0 * M_PI * (ib - 1.0) / Nblades;
33  psi = angvel*time+phase;
34
35  theta = th0 + th1c*cos(psi) + th1s*sin(psi);
36  beta = bt0 + bt1c*cos(psi) + bt1s*sin(psi);
37  lag = lg0 + lg1c*cos(psi) + lg1s*sin(psi);
38
39  thetadat = -th1c*angvel*sin(angvel*time+phase) + th1s*angvel*cos(
        angvel*time+phase);
40  betadat = -bt1c*angvel*sin(angvel*time+phase) + bt1s*angvel*cos(
        angvel*time+phase);
41  lagdat = -lg1c*angvel*sin(angvel*time+phase) + lg1s*angvel*cos(
        angvel*time+phase);
42  . . . Shortened version . . .
```